UC Santa Barbara
UC Santa Barbara Electronic Theses and Dissertations

**Title**
Quantifying the forces that drive zebrafish axis elongation and somitogenesis

**Permalink**
https://escholarship.org/uc/item/70z0q6cn

**Author**
Shelton, Elijah Robinson

**Publication Date**
2021

**Supplemental Material**
https://escholarship.org/uc/item/70z0q6cn#supplemental

Peer reviewed|Thesis/dissertation

eScholarship.org Powered by the California Digital Library
University of California

University of California
Santa Barbara

# Quantifying the forces that drive zebrafish axis elongation and somitogenesis

A dissertation submitted in partial satisfaction
of the requirements for the degree

Doctor of Philosophy
in
Mechanical Engineering

by

Elijah Robinson Shelton

Committee in charge:

Professor Otger Campàs, Chair
Professor Frederic Gibou
Professor Robert McMeeking
Professor Sebastian Streichan

June 2021

The Dissertation of Elijah Robinson Shelton is approved.

Professor Frederic Gibou

Professor Robert McMeeking

Professor Sebastian Streichan

Professor Otger Campàs, Committee Chair

March 2021

Quantifying the forces that drive zebrafish axis elongation and somitogenesis

Copyright © 2021

by

Elijah Robinson Shelton

For Tessa

# Acknowledgements

I am incredibly grateful for the support and guidance of my advisor, Otger Campàs. Thank you for your continued encouragement, confidence, and mentorship over all these years.

I would like to thank my thesis committee members Robert McMeeking, Frederic Gibou, and Sebastian Streichan.

I would like to thank Kevin Plaxco and Sumita Pennathur, for their mentorship and guidance.

I would like to thank all the funding agencies which have supported me and this work.

It has been a joy to work with all members of the Campas lab, including Ale, Friedhelm, Jamie, Adam, Mishel, Samhita, James, David, Hannah, Carlos, Dennis, Yucen, Renwei, Georgina, Marie, Antoine, Shuoting, and both Bens. A big thank you to anyone who spent some time in the fish room, especially those who helped keep the experiments going during Covid restrictions.

I would like to thank the staff of the Animal Research Facility, the Center for Nanosystems Institute, the Bioengineering Building, the Institute for Collaborative Biotechnologies, and the mechanical engineering department. A special thank you to the building committees who coordinated the research ramp up plans during the pandemic.

I thank my family who has always encouraged and supported me through these many years. I can't wait to hug you all again.

Lastly, I thank my partner Tessa, who has seen me through every high and low. Looking forward to our first dance as doctor and doctor!

# Curriculum Vitæ

Elijah Robinson Shelton

519 $\frac{1}{2}$ Fig Ave, Santa Barbara, CA 93101
eshelton@ucsb.edu ●

## EDUCATION

| | |
|---|---|
| **2012 - 2021** | **University of California, Santa Barbara**<br>Ph.D. in Mechanical Engineering March 2021<br>Doctoral Advisor: Otger Campàs |
| **2007 - 2011** | **Brown University**<br>Sc.B. in Physics, May 2011<br>Advisor: Derek Stein |

## RESEARCH

| | |
|---|---|
| **2014 - 2021** | **University of California, Santa Barbara**<br>Graduate Student Researcher<br>Otger Campàs Laboratory |
| **2012 - 2014** | **University of California, Santa Barbara**<br>Graduate Student Researcher<br>Sumita Pennathur Nanofluidics Laboratory |
| **2011 - 2012** | **University of California, Santa Barbara**<br>Academic Coordinator and Assistant Specialist<br>Sumita Pennathur Nanofluidics Laboratory |
| **2009 - 2011** | **Brown University (Providence, RI)**<br>Undergraduate Researcher<br>Derek Stein Nanobiophysics Group |
| **Jun 2010** | **Universität Augsburg (Augsburg, Germany)**<br>Research Intern (4 weeks)<br>Experimentalphysik I |
| **Jun - Aug 2009** | **University of California, Santa Barbara**<br>Research Assistant<br>Phil Lubin Experimental Cosmology Group |

## AWARDS & HONORS

| | |
|---|---|
| **TOTAL:** | **$167,319** ($157,319 stipends, $10,000 research funds) |
| **May 2018** | **Departmental Summer Research Fellowship**<br>$7,200 stipend |
| **Sep 2016** | **University of California Doctoral Scholars Fellowship**<br>$24,000 stipend |
| **Aug 2015** | **Mellichamp Fellowship for Graduate Students in Systems Biology and Bioengineering**<br>$10,000 research funds |
| **2012 - 2015** | **Nat'l Science Foundation Graduate Research Fellowship**<br>$103,000 stipend |
| **2012 - 2015** | **Santa Barbara Foundation Scholar** (multiple awards)<br>$17,619 stipend |
| **Mar 2010** | **W&F Hewlett Undergraduate Teaching and Research Award**<br>$3,000 stipend |
| **Apr 2009** | **Fisher Family Endowed Internship Award**<br>$2,500 stipend |

## PUBLICATIONS

*Peer Reviewed Journals*

1. **ER Shelton**, S Kim, BJ Gross, R Wu, M Pochitaloff, I Lim, E.M. Sletten, O. Campàs. Stress-driven tissue fluidization physically segments vertebrate somites (In preparation).
2. BJ Gross, **ER Shelton**, C Gomez, O Campàs Automated geometrical characterization of deformable particles for *in vivo* measurements of cell and tissue mechanical stresses. *bioRxiv* (2021).
3. A Mongera, P Rowghanian, HJ Gustafson, **ER Shelton**, DA Kealhofer, EK Carn, F Serwane, AA Lucio, J Giammona, O Campàs. A fluid-to-solid jamming transition underlies vertebrate body axis elongation *Nature* 561, 401-405 (2018)
4. **ER Shelton**, F Serwane, O Campàs. Geometrical characterization of fluorescently labelled surfaces from noisy 3d microscopy data. *Journal of Microscopy* 269 (3), 259-268 (2018)
5. AA Lucio, A Mongera, **ER Shelton**, R Chen, AM Doyle, O Campàs. Spatiotemporal variation of endogenous cell-generated stresses with 3D multicellular spheroids. *Scientific Reports* 7 (1), 12022 (2017)
6. **ER Shelton**, Z Jiang, S Wang, D Stein. Controlling the Conformations and Transport of DNA by Free Energy Landscaping. *Applied Physics Letters* 99, 263112 (2011)

## PRESENTATIONS AND POSTERS

1. Stochastic Physics in Biology, Gordon Research Conference, Poster Session, Ventura, CA, January 2019
2. Biophysical Society 62nd Annual Meeting, Poster Session, San Francisco, CA, February 2018
3. Max Planck Institute for Intelligent Systems, J Spatz Group Meeting, Invited Presentation, Stuttgart, Germany, December 2017
4. Southern California Zebrafish Meeting, Presentation, Los Angeles, CA, December 2017
5. American Physical Society March Meeting, Abstract No. A35009, Presentation, Baltimore, MD, March 2016
6. American Physical Society 65th Annual Division of Fluid Dynamics Meeting, Poster Session, San Diego, CA November 2012
7. Southern California Symposium on Flow Physics (6th), Presentation, Santa Barbara, CA, April 2012
8. National Science Foundation Engineering Education Conference, Poster Session, Arlington, VA, March 2012
9. Fall Meeting of New England Section of the American Physical Society, Poster Session, Providence, RI, October 2010
10. Brown University Summer Research Symposium, Poster Session, Providence, RI, August 2010

## TEACHING

| | |
|---|---|
| **Fall 2013** | **Teaching Assistant for ME 291A (Electricity and Magnetism)**<br>Presented lectures, developed problem sets, graded assignments |
| **2012 - 2019** | **Private Tutor**<br>Advanced Placement (AP) courses, including Physics, Calculus, Statistics, and Chemistry |

## MENTORING

| | |
|---|---|
| **2019 - 2020** | **Ray Wu**<br>Undergraduate Researcher<br>Campas Group, UC Santa Barbara |

| | |
|---|---|
| **2017 - 2018** | **Gautam Bordia**<br>Undergraduate Researcher<br>Campas Group, UC Santa Barbara |
| **2012 - 2013** | **Dean Wink**<br>Undergraduate Researcher<br>Pennathur Group, UC Santa Barbara |
| **2010 - 2011** | **William Poole**<br>Undergraduate Researcher<br>Stein Group, Brown University |

# Abstract

Quantifying the forces that drive zebrafish axis elongation and somitogenesis

by

Elijah Robinson Shelton

The study of morphogenesis in animals is concerned with the question of how the structures composing the body acquire their form during embryonic development. As cells are able to sense and respond to biochemical as well as physical cues, a complete understanding of any morphogenetic process requires an understanding of genetic as well as mechanical factors at play. While many powerful tools have been developed for studying and manipulating genetics, the set of tools able to probe the mechanics of living systems is rather limited. In this thesis, I present my contributions to the technological advancement of droplets as *in vivo* and *in situ* mechanical sensors, as well as a series of measurements in zebrafish embryos characterizing stress patterning during two hallmark morphogenetic events: body axis elongation and somitogenesis. I discuss how these stress measurements, along with other quantifications, yield new insights into physical mechanisms underlying both body axis elongation and somite formation.

First, I discuss the development of a computational tool for automated surface analysis of volumetrically imaged particles which have been surface-coated with a fluorescent label. Prior to this work, droplets as force sensors had been developed as a proof-of-principle technology, but no framework for automated and accurate segmentation of a droplet surface and quantification of its surface curvature had been developed. Since droplet stress sensors work by relating anisotropies in surface normal stress to the observed variations in mean curvature on the droplet surface and a known value of surface interfacial tension, an automated method of transforming image data into stress measure-

ments is required for any large scale implementation of the technique. Here, I demonstrate such an algorithm and characterize the performance in terms of accuracy on simulated and experimental data sets.

Next, I discuss a collaborative study of the mechanical conditions underlying body axis elongation in zebrafish. Here, I present droplet-based measurements of cell-scale and tissue-scale stress collected in the mesodermal progenitor zone (MPZ) and along the presomitic mesoderm (PSM) in zebrafish embryos at 10 somites stage. I show that local patterns of cell-scale stress are correlated on short timescales ( 1 minute), while the amplitudes of these stresses are spatially uniform from the MPZ to the PSM. In contrast, tissue scale stresses increase from the posterior to the anterior end of the tissues. I also discuss these stress measurements in the context of experiments showing the existence of a spatially graded yield stress in the tissue. I explain how the regional tuning of cell-cell junctional tension fluctuations, cell volume fraction, and large-scale stresses gives rise to a rigidity gradient, which helps to explain how body axis elongation occurs.

Finally, I explore a puzzle introduced by the findings of the previous chapter: how are somites mechanically sculpted from the recently rigidified PSM? I motivate a mechanical model for somite boundary formation with experiments and simulation. Using live imaging, I quantify the morphological dynamics of somite boundary formation, and relate the time evolution of boundary straightening to the time evolution of enrichment of F-actin and myosin II at the forming border. To understand how stresses change over the formation period, I collect time course measurements of cell and tissue scale stresses using droplets. Here, we find average cell-scale stresses show no significant change, while tissue scale stress anisotropies re-orient and increase in amplitude as somite boundaries form. I also analyze the spatiotemporal distributions of T1 transition rates within a forming somite, and I discover a spatial gradient in the rates of cell-cell rearrangements. These experimental findings, in combination with simulations, suggest that increased actomyosin activity drives increases in tension at the nascent boundary, resulting in localized fluidization, allowing the somite to rapidly section off from the PSM.

Taken together, the years of research presented here demonstrate the value of droplet force sensor technology as a powerful tool for gaining insights into the physical mechanisms which guide morphogenesis. In case of axis elongation, we learned how fluctuating stresses at cellular scales tune material properties to allow uniaxial growth at the posterior end. In the case of somitogenesis, we learned how acute increases in stress anisotropies locally fluidize boundaries and enable physical segmentation of somites. In my final chapter, I reflect on my cumulative findings and discuss possible future directions of research.

# Contents

**Curriculum Vitae** **vi**

**Abstract** **x**

**1 Introduction** **1**
1.1 A Brief History of Morphogenesis . . . . . . . . . . . . . . . . . . . . . 3
1.2 Experimental Toolbox of the Mechanobiologist . . . . . . . . . . . . . . 11
1.3 Outline . . . . . . . . . . . . . . . . . . . . . . . . . . . . . . . . . . . 15

**2 Geometrical characterization of fluorescently labelled surfaces from noisy 3D microscopy data** **18**
2.1 Background . . . . . . . . . . . . . . . . . . . . . . . . . . . . . . . . . 18
2.2 Surface Segmentation: Generating the Point Cloud . . . . . . . . . . . . 20
2.3 Measuring Curvature from the Point Cloud . . . . . . . . . . . . . . . . 23
2.4 Testing Accuracy with Model Objects . . . . . . . . . . . . . . . . . . . 26
2.5 Analysis of Experimental Data . . . . . . . . . . . . . . . . . . . . . . . 33
2.6 Conclusions . . . . . . . . . . . . . . . . . . . . . . . . . . . . . . . . . 37
2.7 Permissions and Attributions . . . . . . . . . . . . . . . . . . . . . . . 38

**3 Mechanical stresses guiding body axis elongation in zebrafish** **39**
3.1 Introduction . . . . . . . . . . . . . . . . . . . . . . . . . . . . . . . . . 39
3.2 Results . . . . . . . . . . . . . . . . . . . . . . . . . . . . . . . . . . . . 40
3.3 Discussion . . . . . . . . . . . . . . . . . . . . . . . . . . . . . . . . . . 43
3.4 Methods . . . . . . . . . . . . . . . . . . . . . . . . . . . . . . . . . . . 45
3.5 Author contributions . . . . . . . . . . . . . . . . . . . . . . . . . . . . 51
3.6 Permissions and Attributions . . . . . . . . . . . . . . . . . . . . . . . 51

**4 Mechanics of Vertebrate Somite Formation** **53**
4.1 Introduction . . . . . . . . . . . . . . . . . . . . . . . . . . . . . . . . . 53
4.2 Results . . . . . . . . . . . . . . . . . . . . . . . . . . . . . . . . . . . . 55
4.3 Discussion . . . . . . . . . . . . . . . . . . . . . . . . . . . . . . . . . . 65
4.4 Acknowledgements . . . . . . . . . . . . . . . . . . . . . . . . . . . . . 67

4.5 Author Contributions . . . . . 68
4.6 Methods . . . . . 72
4.7 Permissions and Attributions . . . . . 80

**5 Final Remarks and Future Directions** **81**
5.1 Final Remarks . . . . . 81
5.2 Future Directions . . . . . 84

**Bibliography** **85**

# Chapter 1

# Introduction

The study of morphogenesis is concerned with the biological processes whereby organisms acquire their forms [1]. In the case of multicellular organisms, the process of autonomously transforming a single cell into a complex three-dimensional architecture of differentiated tissues, organs, and organ systems requires an astounding level of spatial and temporal coordination in the directing of cell fates and tissue movements. Since Turing first proposed the concept of morphogens in 1952[2] , biochemical signaling has been well studied as a mechanism by which tissues and organs are patterned[3]. However, we now understand cells have the ability to sense and to respond to mechanical cues in addition to biochemical signals[4]. Moreover, the patterns of strain (i.e. cellular and tissue movements) involved in morphogenesis ultimately have physical origins. In recognizing that morphogenesis emerges from the interplay of biochemical and mechanical factors, we must also acknowledge that a holistic understanding of morphogenesis is incomplete without an understanding of the forces generated within the developing embryo.

Despite the significant role mechanical forces play in the sculpting of tissue, few techniques exist that allow us to study forces or to measure mechanical properties within living systems. Many of the techniques that do exist, such as atomic force microscope

(AFM) or Brillouin microscopy, have significant drawbacks. Oil droplet force sensors are a recently developed technology well suited to the task of characterizing stresses inside living tissues[5]. Oil droplets are mechanically responsive at physiologically relevant time scales, they can be tuned to length scales suitable to their the system, they can be inserted into intact living tissue, and they provide a true three-dimensional readout of stresses. However, in order to employ this technique efficiently on a larger scale, we need automated image analysis and surface analysis tools that can translate volumetric images of droplets into useful mechanical measurements. In chapter 2, I present my work developing an automated computational analysis tool that makes these necessary advances in droplet force sensor technology.

The ability to investigate how mechanical stresses are spatially and temporally patterned within embryonic tissues can help us to understand the physical mechanisms underlying various motifs in morphogenesis. This thesis explores two hallmark morphogenetic events in vertebrates: axis elongation and somitogensis. During development vertebrate body is segmented along its long axis into clusters of cells called somites, which form head to tail as the body grows posteriorly. These segments of tissue give rise to segmented muscle and skeleton in adults. The speed at which the body axis extends and the rate at which somites progressively form are tightly coordinated with one another so as to determine the number of segments particular to a species as well as the overall body axis length. While cellular behaviors have been observed and many key molecular players identified [6], the mechanical stresses underlying these processes have been unknown prior to the work discussed in this thesis. In chapter 3, I present measurements of cell and tissue scale stress along the anterior-posterior axis of zebrafish embryos at 10 somite stage. I show that cell-scale stresses are uniform and temporally short-lived (on the order of 1 minute), while tissue-scale stresses increase in magnitude from posterior to anterior and persist for over longer timescales ($> 30$ minutes). In chapter 4, I present time series measurements of stresses generated during somite formation. I also show how these stresses correlate with increasing concentrations in force-associated proteins, F-actin and myosin II, at the forming somite boundary.

In my final chapter, I discuss the significance of all these findings and consider opportunities for future investigations. Mechanobiological investigations of morphogenesis and other biological phenomena is an exciting and still developing field. Before presenting my own contributions to this field, I shall put them within a larger context of the history of evolutionary developmental biology.

## 1.1 A Brief History of Morphogenesis

### 1.1.1 Aristotle to D.W. Thompson.

Morphogenesis, or the origin of biological form, has long been a subject of interest and inquiry among scientists. Western thought on animal morphogenesis can be traced back at least as far as 2500 years to Aristotle's *Generation of animals*, in which he considers, through observation and reason, the possible mechanisms underlying embryogenesis. Some notions expressed by Aristotle, such as spontaneous generation (i.e. flies generated *de novo* within dead animal carcasses), have since been abandoned. Other theories posed by Aristotle feel prescient even today. For example, he argued that development occurs through a collection of events unfolding in particular sequence set into motion by fertilization which transform the material components of the egg into some defined form. Aristotle's mechanistic view of development, which he compared to the automatons of the Greek temple [8, 9], would inform two competing philosophies of morphogenesis which emerged in the ensuing millenia: preformationism, in which an organism's form is ever present, even at the very "beginning", and epigenesis, in which form emerges from

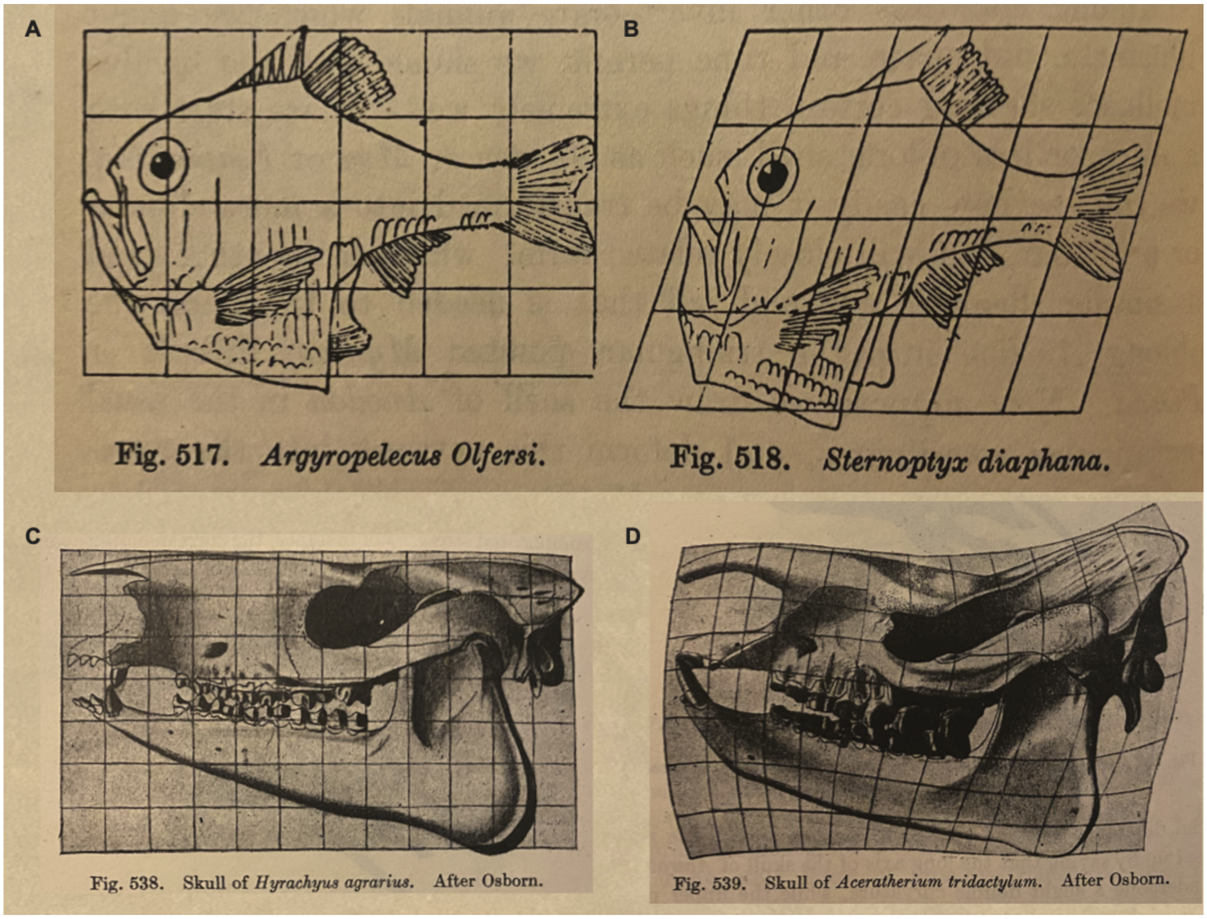
A
B
Fig. 517. Argyropelecus Olfersi.
Fig. 518. Sternoptyx diaphana.
C
D
Fig. 538. Skull of Hyrachyus agrarius. After Osborn.
Fig. 539. Skull of Aceratherium tridactylum. After Osborn.

Figure 1.1: **D'Arcy Thompson's Theory of Transformations, or The Comparison of Related Forms.** By simple shear, Thompson demonstrates how the form of **A**, *Argyropelecus Olfersi*may be transformed into the **B**, Sternoptyx diaphana. A more complex transformation is used to related **C**, the skull of the extinct rhinoceros *Hyrachyus agrarius* to **D**, the skull of the extant *Aceratherium tridactylum.* (Adapted from [7])

organizational events over time [10].

While philosophical debates between preformationists and epigenecists continued through the 17th, 18th, and 19th centuries, experimental advancements in microscopy technology allowed new direct and more detailed observations of embryonic development. The debates of the 19th century did spur on significant investigations, leading to new discoveries, but they did not lead to a consensus between the two sides. For instance, while August Weismann and Oscar Hertwig agreed that all individuals come from cells that contain hereditary material in the nuclei, they took fundamentally different positions on whether development and differentiation was directed by inheritance (Weismann's preformationism) or arose from the interactions among cells and the differences between them (Hertwig's epigenesis) [10]. When Roux observed that a frog embryo will proceed to develop as a half-frog embryo when one cell is destroyed after the first division, this was presented as evidence for the preformationist's predetermined mosaic hypothesis[11]. When Driesch showed that cells from the sea urchin, when separated after one or two divisions, retained their potency to develop into complete organisms, he saw evidence to reject the mosaic hypothesis and embrace epigenesis[12]. By the start of the 20th century, work by Charles Otis Whitman, Edmund Beecher Wilson and others at the Marine Biological Laboratory at Woods Hole, Massachusetts suggested a compromise view in which development was largely an epigenetic process with some predeterminism; nuclear material in the fertilized egg was preorganized in the chromosomes, but cells still maintained an ability to respond to environmental factors and regulate themselves. [10].

The debates between between preformationists and epigenecists of the 19th century were happening in the context of evolutionary debates between Jean-Baptiste Lamarck and Charles Darwin. Larmarck proposed an evolutionary theory in which a complexifying force drives body plans up a ladder of progress and an adaptive force drives variation between species. This adaptive force alllows animals animals to obtain or lose features either through use or disuse, or through inheritance of characteristics acquired from environmental influence[13]. Darwin pointed to observations that some animals whose adult forms differed greatly possessed quite similar embryonic forms during development as evidence for his theory of evolution by natural selection and gradual change by descent[14]. Ernst Haeckel, an advocate of scientific racism and eugenics, attempted to unify Lamarckism, Darwinism and embryology with a “biogenetic law” in which animals evolve and devolve along a hierarchy and the history of ancestral adult forms is reflected in their development[15]. In asserting that ontogeny recapitulates phylogeny, Haeckel embraced a kind of figurative preformationism (or predeterminism), in which the animal’s shape is not determined through interactions within the egg, but is predetermined by the evolutionary history. Haeckle represents an effort to use the 19th century frameworks of preformationism and epigenetics to understand the relationship between the evolution of an organism and development of an embryo. However, the mechanisms underlying this unification, molecular genetics, would not be clearly elucidated until the mid to late 20th century.

The modern synthesis of the early 20th century created a framework for unifying Darwinian evolution with Mendelian inheritance, but failed to unify embryology and evolutionary biology. When D’Arcy Thompson publishes *On Growth and Form*[7] in 1917, exploring the mathematical and mechanical explanations for animals’ forms (fig1.1), the work seems to have managed to arrive both too late and too early: too late, in that this ideas were not easily incorporated into the genetic evolutionary biology of the day, and too early, in that many of the mathematical and technological tools to required engage in the question of a mechanical explanation for biological form were not yet available. *On Growth and Form* was well received upon its initial publication, and the ideas presented within influenced scholars throughout the 20th century. However, it is only in recent decades that an alliance between physicists, engineers, and biologists has formed able to articulate and engage the mechanical framework of morphogenesis put forth by Thompson.

### 1.1.2 20th Century: From Modern Synthesis to Evo-Devo.

The twentieth century witnessed remarkable advancements in our understanding of genetics and its relationship to heredity and development. In 1911, Morgan proved that genetic material is carried on the chromosomes through his work with fruit flies [16]. It was suggested by Frederic Griffith's experiment in 1928 [17] and later confirmed by Avery and colleagues in 1943 that DNA, not proteins as popularly suspected, carried genetic information capable of transforming bacteria [18]. With the Hershey-Chase experiments of 1952, the case for DNA as the hereditable genetic material was solidified [19]. The same year, the famous X-ray diffraction image "Photo 51" was taken by graduate student Raymond Gosling, working under Rosalind Franklin, which aided in the discovery of the double helical structure of DNA in 1953 by James Watson and Francis Crick[20, 21]. Crick laid out the "central dogma" of molecular biology in 1957, and the supposed mechanism of replication suggested by DNA's double helix was confirmed by the Meselson-Stahl experiment in 1958. In 1961, Crick, Brenner, et al. showed codons indeed consist of three base pairs[22], and the nature of how these genetic codons were deciphered into amino acid sequences was further clarified throughout the 1960s, with a 1968 Nobel prize in medicine awarded to Khorana, Holley, and Nirenberg. Entering the latter half of the 20th century, it was very clear that DNA contained important information which played a role in specifying an organism's phenotype, including its shape. However, the mechanisms by which genetic factors orchestrated the morphogenetic sculpting of an embryo were not clear in the 1960s.

New ideas and discoveries in the later part of the 20th century would ultimately bring embryology and molecular genetics, phylogeny and evolutionary biology together. The same year that Gosling took the exposure of "Photo 51", Alan Turing, while undergoing forced chemical castration as a condition of his probation[1], published *The Chemical Basis of Morphogenesis*. In this work, he explains how reaction-diffusion mechanisms generate self-organizing patterns, and coins the term "morphogen" to describe a diffusing agent capable of specifying positional information within the developing embryo in a concentration dependent manner. Then in 1961, Monod, Changeux, and Jacob demonstrated that genes can be regulated in their discovery of the lac operon in *E. coli*[23]. Three significant works appear in 1977 [24, 25, 26], causing some to declare it the year of Evo-Devo's conception [27]. In *Ontogeny and Phylogeny* [24], Stephen J. Gould critiques and condemns Haeckel's racist and unscientific biogenetic law, and identifies the need for a new framework for unifying evolution and development. In his essay *Evolution and Tinkering* [25], François Jacob offers such a counter-framework to the Haeckelian evolutionary ladder; rather than an ascendent progression upward towards higher forms of being, evolution creates a web of life through a "tinkering" process in which the particular results the consequence of an arbitrary history. In Maxam and Gilbert's "A new method for sequencing DNA" we see an example of the kinds of new genetic tools being developed[26] which would empower biologists to explore within the Jacobian tinkering paradigm.

New ideas combined with new technologies (i.e. recombinant DNA) led to transformative discoveries. Homeobox genes identified in flies [28] and later in vertebrates led to the realization that embryonic development unfolds under the guidance of toolkit genes which are ancient and conserved across different animals. For example, *Hox* genes are involved in anterior-posterior specification, *Pax6* genes specify photoreceptor and eye development, and *Nkx2.5* genes guide heart formation[27]. By the end of the twentieth century, the picture of evolutionary developmental biology was thus: different animals are "constructed" using the same set of genetic programs activated during development which direct induction and differentiation of cell fate, as well as cellular and tissue movements. Instead of analogizing with the ancient Greek automata as Aristotle had, biologists of the day imagined a set of deterministic genetic programs running within cells, similar to the set of software programs running on their computers. Evolution occurs through historic mutations which perturb these genetic networks, modifying the targets of signaling paths or the spatiotemporal patterns of expression, leading eventually to the diverse web of life, and their respective forms, which we see today.

---

[1] Turing was charged with "gross indecency" after acknowledging a same-sex relationship. He was offered the choice of imprisonment or probation, and selected the latter. In 2013, he was posthumously pardoned by the Queen.

### 1.1.3 A Mechanobiological Morphogenesis.

In recent decades, the idea that cell fates and movements are directed by genes in a top-down fashion has fallen to the wayside[3, 4]. The contemporary view is that changes occuring during development generate physical cues which are integrated along with biochemical signals by cells in order to robustly guide tissues in their growth and morphogenesis. Among the significant body of research that has advanced this perspective in the field, the contributions of Lance Davidson, Celeste Nelson, Thomas Lecuit, C.P. Heisenberg, and Suzanne Eaton are particularly noteworthy.

While various models for the mechanisms underlying morphogenetic events have been proposed over the years, the development of computational and experimental tools in recent decades has allowed researchers to generate and test hypothesis in a methodical way. For example, in 1995 Davidson and colleagues used finite element simulations of sea urchin invagination to generate the testable predictions associated with the various proposed models. In 1999, Davidson and colleagues used these predictions from simulation to dismiss certain morphogenetic models as physically implausible based on mechanical measurements of sea urchin blastula wall [29].

Advances in fluorescence microscopy, and in particular live-imaging of fusion proteins, have significantly improved the study of in vivo cell movements and the mechanisms underlying such movements. Through live imaging of Drosophila germ band extension, Claire Bertet, Lawrence Sulak, and Thomas Lecuit demonstrated that axis elongation occurs through planar cell intercalation which is driven by the polarized localization of myosin II at cell-cell boundaries[30]. In their 2012 study of epithelial spreading in zebrafish gastrulation, Martin Behrndt and colleagues[31] used live-imaging of actin flows, in conjunction with laser ablation measurements and an elegant experiment in which a gastrulating embryo is geometrically constrained within a cylindrical tube, to demonstrate that forces driving tissue movements consist of both a contractile actomyosin ring, as well as a flow-friction mechanism.

Work by Nelson and colleagues demonstrated that geometry itself, not just genetic factors, could play a role in regulating growth. [32]. By culturing cells in micro-patterned regions of various shapes, they showed that the geometry of tissues themselves could provide a feedback specifying patterns of growth. Using finite element modeling and traction force measurements, they learned that regions with higher rates of proliferation corresponded to regions of higher stress. Through inhibition of actomyosin or cadherin, it was determined that mechanical stresses provided the physical cues connecting tissue form to patterns of growth. Additional research explored the implications of such feedback mechanisms on branching morphogenesis [33]. The idea that forces themselves can play a regulatory role was further supported by in vivo studies showing that, at pupal stages, wing hinge contraction realigns planar polarity of cells in Drosophila, and, during germ band elongation, tension in intercalating cells plays a role in recruiting and stabilizing myosin II at cell cortices.

There is not room here, nor is it the intent, to chronicle all the works which have led to the contemporary understanding that development occurs through an interplay of genetic and physical factors. Beyond the works referenced above, there is mounting evidence to suggest mechanical forces play a significant role in regulating and guiding morphogenetic processes[34, 35, 4, 3]. Instead of imagining a hierarchy of instruction in which genetic scripts direct cells to carry out actions that shape embryos, we should instead picture cells as guided by an interplay of mechanical and biochemical cues. The question of how this occurs is the purview of "mechanical biology," which has taken up the mantle of D'Arcy Thompson by recruiting thinking from developmental biology, engineering, and physics[3, 4].

In this contemporary picture of morphogenesis, we are encouraged to take a holistic view. Understanding a morphogenetic process demands both an understanding of the genes regulating it, as well as the forces generated between cells and within tissues which drive cell and tissue movements, and in some cases play a regulatory role as well. In order to investigate the patterns of stress developing within embryos, mechanobiologists need experimental tools suitable for characterizing the mechanical aspects of biological tissues.

## 1.2 Experimental Toolbox of the Mechanobiologist

While many tools exist for studying the genetic factors at play in embryonic developement, relatively few tools have been developed for studying the mechanical aspects of biological tissues[39]. Many of the tools that do exist, such as laser ablation, Brillouin microscopy, or atomic force microscopy (AFM) have significant limitations[39, 40]. In contrast, droplet-based force sensors are uniquely suited for *in situ* and *in vivo* investigations of cellular and tissue scale mechanics[5].

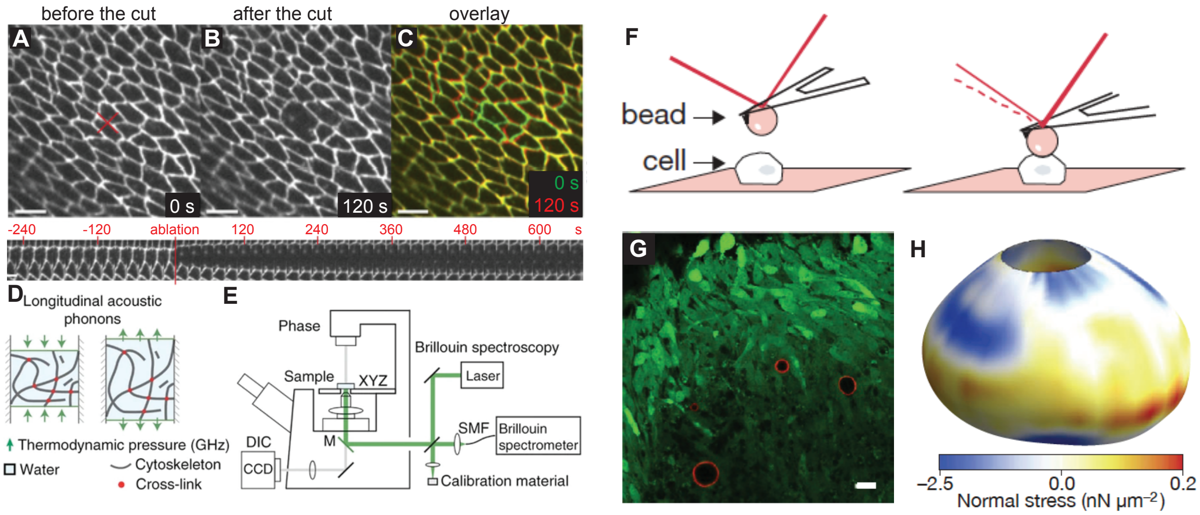
before the cut
after the cut
overlay
A
B
C
0 s
120 s
0 s
120 s
-240
-120
ablation
120
240
360
480
600
s
D
Longitudinal acoustic phonons
Thermodynamic pressure (GHz)
Water
Cytoskeleton
Cross-link
E
Phase
Sample
XYZ
Brillouin spectroscopy
Laser
SMF
Brillouin spectrometer
DIC
M
CCD
Calibration material
F
bead
cell
G
H
−2.5
0.0
0.2
Normal stress (nN μm⁻²)

Figure 1.2: **Experimental tools for studying mechanics in biological systems** **A-C**, Before (**A**) and after (**B**) pulsed laser removal of cell contact. When parts of cells or tissues are removed by laser ablation, relaxation of mechanical stresses results in a local rearrangement of cells, which may be observed (Adapted from [36]). **D-E**, Brillouin microscopy uses photon scattering to interrogate a sample's effective longitudinal modulus (Adapted from [37]). **F**. Atomic force microscope cantilever, adapted for studying the mechanical properties of a single cell (Adapted from [38]). **G-H**, Fluorocarbon oil droplets adopt deformations in response to stresses present in the local cellular environment (**G**). Anisotropies in surface normal stress can be quantified from the local surface mean curvature and the droplet's interfacial tension (**H**) (Adapted from [5]).

### 1.2.1 Laser ablation.

Laser ablation (fig. 1.2a-c) works by delivering a large amount of power to a region of tissue via focused light, thus ablating (destroying) an area of interest [41, 40]. When mechanically-loaded features are destroyed in the ablation event, stresses and strains will reorganize accordingly. Destroying tissue via the ablation event allows researchers to observe the rearrangement of cells and measure retraction velocities. However it is impossible to map the observed retraction velocities obtained from laser ablation to measurements of stress without making assumptions about the mechanical properties of the tissue under interrogation. In addition to not being a quantitative tool for measuring absolute stresses, the destructive nature of laser ablation makes it impossible to perform success measurements on the same sample.

### 1.2.2 Brillouin microscopy.

Brillouin microscopy (fig. 1.2d,e) works through the mechanical interaction of light with the sample of study. Brillouin scattering is able to characterize a material's apparent longitudinal modulus in 2D and 3D, and it has been used to measure the hydromechanical properties in intracellular and extracellular regions *in vitro* [37], and *in vivo* [42]. Brillouin scattering is, however, significantly limited by the fact that it only measures high frequency material responses and is only suitable for characterizing mechanics at short time and length scales. Brillouin scattering cannot yield insights into cytoskeletal network tension or cortical contractility. It is unclear to what extent high frequency longitudinal modulus characterizations correlate with physiologically relevant tissue mechanical properties.

### 1.2.3 Atomic force microscopy.

AFMs are capable of both applying and measuring minute levels of stress and strain (fig. 1.2f). For this reason, they are suitable to measuring physiologically relevant stresses and strains[38]. Unfortunately, AFMs are only able to access and probe surfaces, making them unsuitable for characterizating internal stresses within intact embryonic tissue.

### 1.2.4 Droplet-based force sensors

Droplet-based force sensors (fig. 1.2g,h) are powerful tools for measuring physical stresses and characterizing mechanical responses *in vitro* within cell aggregates or *in vivo* within embryonic tissues. Droplets of fluorocarbon oil are inserted into tissue samples where they adopt a shape in accordance with the cellular and tissue stresses acting on it. If the droplet is loaded with a fluorescent marker, either through a surface label or a fluorocarbon soluble dye, the shape can be imaged with a microscope. To transform the droplet image into a stress measurement, the geometry of the droplet surface must be extracted and quantified from the image, and then the local surface curvature may be related to anisotropies in surface stresses if the droplet interfacial tension is known. Droplet interfacial tension may be determined by pendant drop, or, if the droplet is magnetically responsive (i.e. ferrofluid), it may be calibrated *in situ* through magnetic actuation with a controlled stress. Unlike AFM, droplet-based measurements are fully 3D. Unlike Brillouin microscopy, droplet-based measurements are sensitive to mechanical stresses at physiologically relevant length scales and time scales. Although the incompressible nature of oil makes it impossible to measure changes in isotropic stress within the droplets, the technology is much simpler to calibrate than techniques like elastic hydrogel microparticles since droplet measurement calibration only depends on interfacial tension.

## 1.3 Outline

In this thesis I describe my work using oil droplet force sensors to advance our mechanobiological understanding of morphogenesis through experimental studies of the physical forces at play during morphogenetic processes. In chapter 2 of this thesis, I present work on a computational tool which supports technology enabling measurement of physical stresses within the tissue of developing embryos. I also present two projects in which we use droplet force sensing technology to directly measure stresses in the developing zebrafish embryos. In chapter 3, I explore the physical mechanisms underlying body axis elongation by characterizing the stress patterning in the mesodermal progenitor zone (MPZ) and presomitic mesoderm (PSM). In chapter 4, I explore the mechanics of somite formation, including a direct measurement of the stresses generated at the forming at the somite boundary.

### 1.3.1 Geometrical characterization of fluorescently labelled surfaces from noisy 3D microscopy data

In chapter 2, I present a fully automated algorithm to determine the location and curvatures of an object from 3D fluorescence images, such as those obtained using confocal or light-sheet microscopy. The algorithm reconstructs surface labelled objects with spherical topology and mild deformations from the spherical geometry with high accuracy, rather than reconstructing arbitrarily deformed objects with lower fidelity. Using both synthetic data with known geometrical characteristics and experimental data of spherical objects, we characterize the algorithm's accuracy over the range of conditions and parameters typically encountered in 3D fluorescence imaging. We show that the algorithm can detect the location of the surface and obtain a map of local mean curvatures with relative errors typically below 2% and 20%, respectively, even in the presence of substantial levels of noise. Finally, we apply this algorithm to analyze the shape and curvature map of fluorescently labelled oil droplets embedded within multicellular aggregates and deformed by cellular forces.

### 1.3.2 Mechanical stresses underlying body axis elongation in zebrafish

In chapter 3, I demonstrate how droplet stress sensors can be deployed *in vivo* to elucidate the physical mechanisms underlying vertebrate body axis elongation. The vertebrate body axis is constructed from head-to-tail, as cells from the dorsal aspect move ventrally into the mesodermal progenitor zone (MPZ) at the posteriorly-extending tip. As the body extends posteriorly, cells from the MPZ are incorporated into the anteriorly-located presomitic mesoderm (PSM). Using images of droplets placed in the MPZ and PSM, I analyze both cell-scale stresses, and tissue-scale stresses. Cell-scale stresses maintain a constant amplitude from posterior to anterior, but fluctuate on timescales of one minute. Tissue-scale stress anisotropies increase from posterior to anterior and exhibit a preferential alignment with the morphogenetic movement of the tissue. This spatial and temporal characterization of cellular and tissue scale stresses along the anterior-posterior axis provides insights into how the tissues maintain a fluidity-rigidity gradient necessary to enable continuous growth within the framework of a glassy-jamming transition.

### 1.3.3 Mechanics of vertebrate somite formation in zebrafish

In chapter 4, I turn my attention to the process of vertebrate axial segmentation by somite formation. Shaping functional structures during embryonic development requires both genetic and physical control. During somitogenesis, cell-cell coordination sets up genetic traveling waves in the presomitic mesoderm that orchestrate somite formation. While key molecular and genetic aspects of this process are known, the mechanical changes required to shape somites from the presomitic mesoderm (PSM) remain unknown. We show that somites are mechanically sectioned off from the PSM by a large, actomyosin-driven increase in anisotropic stress at the nascent somite-somite boundary by performing direct mechanical measurements during somite formation, live imaging of tissue structure, quantification of morphology and actomyosin dynamics, as well as computer simulations. Our results show that this localized increase in stress drives the regional fluidization of the tissue adjacent to the somite border, enabling local tissue remodeling. Moreover, we find that active tension fluctuations in the tissue are optimized to mechanically define sharp somite boundaries while minimizing somite morphological defects. Altogether, these results indicate the mechanical changes at the somite-somite border and optimal tension fluctuations in the tissue are essential physical aspects of somite formation.

# Chapter 2

# Geometrical characterization of fluorescently labelled surfaces from noisy 3D microscopy data

## 2.1 Background

From medicine to entertainment, industrial design to archeology, there is a long and growing interest in engaging with 3D data captured from real world objects, with methods as varied as the applications. The increasing use of 3D imaging in fluorescence microscopy applications, with confocal microscopy being now mainstream, has allowed for the acquisition of large amounts of 3D data in both biological and physical systems. Examples include biological studies of the morphological changes that occur during cell migration [43, 44], the microbial cell shape [45], the cellular packings during tissue morphogenesis [46, 47] and early embryonic development [48], and even the geometry of the cell nucleus at the subcellular scale [49, 50]. Studies of the mechanics of emulsions in soft-matter physics also rely on the ability to characterize the geometry of individual droplets [51, 52]. Importantly, several new techniques to either measure or infer cellular stresses in 3D multicellular systems require a quantitative measure of surface curvature from 3D fluorescence images. This includes 2D [53] and 3D [54] force inference methods and techniques that use oil droplets [5] or deformable elastic beads [55] to quantify cellular stresses. In all these cases, it is essential to be able to characterize the geometry of the imaged object with sufficient accuracy so that quantitative studies can be performed.

A myriad of customized image segmentation and analysis methods have been developed and used to analyze 3D fluorescence microscopy images. Many computationally efficient algorithms have been developed for detecting interfaces and surfaces, including automated thresholding [56], watershed [57], marching cubes [58] and active contour [59, 60]. Generally, the accuracy of these methods is suitable for most visualization purposes [61] and some quantitative analyses like cell counting and tracking [62]. In some cases, morphology and curvature measurements are possible [63, 64], albeit with relatively low accuracy. Indeed, small errors in surface segmentation can cause significant errors in the analysis of the surface geometry, especially for curvature measurements.

In this chapter, we present an automated algorithm for surface segmentation and curvature characterization, developed using MATLAB (MathWorks). Starting from 3D tiff stacks of isolated objects with a fluorescently-labeled surface, we use a ray-tracing algorithm to detect the location of the surface with high (sub-pixel) resolution and build a point cloud that mathematically represents the object's surface. Since the algorithm relies on raytracing, it can detect the object surface with high precision but it cannot reconstruct objects with very large departures from the spherical geometry, for which the rays would intersect the surface more than once. The local curvature at every point of the surface is then obtained through local quadratic fitting of the surface in a small neighborhood of each point, with a size determined by an adaptive algorithm aimed at minimizing the errors in local curvature measurements. The work is focused on obtaining the surface map of mean curvature, but principal curvatures and Gaussian curvature can also be obtained. Using synthetic data with known geometrical characteristics and experimental data from known objects (droplets), we show that the algorithm is able to locate the surface with sub-pixel precision even in the presence of substantial levels of noise. For the range of imaging parameters explored here, the presented algorithm can detect the location of the surface and local mean curvatures with relative errors below 1.6 % and 12.5 %, respectively. Estimation of errors using synthetic data for a wider range of imaging conditions indicates that the algorithm can detect the surface and obtain its local curvature with relative errors below 2% and 20%, respectively. As proof-of-principle, we use the developed algorithm to analyze the shape and mean curvature map of fluorescently-labeled oil droplets embedded in multicellular aggregates. In this realistic situation, we estimate the relative error in the detection of the surface and the measurement of the mean curvature to be smaller than 2% and 13%, respectively.

## 2.2 Surface Segmentation: Generating the Point Cloud

In order to obtain a mathematical representation of the object's surface in terms of a point cloud (coordinates of surface points), we first manually crop the original image-stack to isolate the object of interest, as the presence of multiple objects too close to each other may cause errors in the reconstruction. If it is not possible to isolate the object of interest by cropping the image volume with a rectangular box, a 3D mask must be manually defined and employed. After isolating the object of interest, the raw images are pre-processed with a 3D median filter to reduce salt and pepper noise levels [65]. In what follows, the filter size is set to 5 by 5 by 5 voxels for images with uniform resolution in $x$, $y$, and $z$. If the voxel size in $x$ ($\ell_x$) is different than the voxel size in $z$ ($\ell_z$), as is often the case for experimental images, the size of the filter is adjusted in $z$ to the nearest odd integer such that the filter's extent in $z$ most nearly approximated the filter's extent in $x$ and $y$. Additionally, images with non-uniform voxel resolution are resampled via cubic interpolation to a higher resolution so as to achieve a uniform $x, y, z$ voxel size. From this new array of intensities, we define a linearly interpolating function that associates any $(x, y, z)$ coordinate in the image volume and to an intensity value.

After resampling the data, it is necessary to locate the fluorescently labeled surface of the object of interest. This is done by tracing line segments (rays) through the image volume and locating peaks in intensity along these rays (Fig. 2.1). This procedure is inspired in single molecule experiments for sub-diffraction-limit localization measurements [66] as well as sub-pixel edge detection algorithms [67]. The major categories of sub-pixel segmentation methods are moment-based, interpolation-based and least-squared-error-based [68]. We choose here to employ a least-squared-error-based method as it has been demonstrated to be the more accurate than other approaches [68]. A similar least-squared-error-based method for segmenting droplets was presented before in 2.5-D, but it was unable to segment closed surfaces properly and its accuracy was not characterized [5]. In addition, this previous 2.5-D algorithm used Steerable filters [69] combined with 2D raytracing for edge detection and obtained in-plane coordinates at each slice. Here we use median filters to significantly reduce background noise in the raw image and use raytracing in full 3D to reconstruct the surface of the object, without making use of Steerable filters. Initially, 100 rays are traced radially outward from an estimated center of the object, which is obtained in a two-step process: First, we calculate the intensity-weighted 3D centroid taken over the entire volume to obtain a rough estimate of the object's center. Second, we perform maximal intensity projections along each axis (x,y,z). On these projections, we trace lines along the remaining axes passing through the projected coordinates of the centroid. By determining the positions of the object boundaries along these lines (via thresholding), we define the new center location on that projection as the point equidistant from the object boundaries along both axes. Rays are then traced out from this center position. The endpoints of these rays are spaced out in the volume according to a golden angle spiral pattern in such a way that the densities of rays are approximately uniform over the object's surface. Intensities along the rays are sampled with $\ell/2$ spatial resolution, using the linearly interpolating function described above. Intensity peaks along the rays are determined through Gaussian fitting, and the positions of the peaks along the rays determine a set of 3D coordinates in the image volume (Fig. 2.1A). This set of point coordinates is used to construct a coarse point cloud model of the object's surface. Since the detection of the interface location relies on raytracing, situations leading to multiple intensity maxima along the rays, such as very deformed surfaces in which rays intersect the surface more than once, cannot be detected properly with this algorithm.

From the initial point cloud, we estimate the surface's ellipsoidal eccentricities, orientation, and surface area. With this new information about the object's size, we increase the number of rays to achieve a desired surface density and retrace them through the volume to achieve nearly even density at the object's surface, with the average distance between neighboring points ($d$) being equal to the voxel size ($\ell$) (Fig. 2.1A). Gaussian fitting along the rays is again used to locate points on the surface and obtain a second, higher density and more uniform, point cloud (Fig. 2.1B). Using this point cloud, we calculate the local normal vector of the surface at each point by diagonalizing the covariance matrix using the coordinates of the 30 points nearest to the point considered. Finally, we retrace all rays through coordinates of the second point cloud along the direction of the local normals to the surface. We again use Gaussian fitting of the intensity profile along the normally-traced rays to obtain our final point cloud. The resulting data set from this procedure is a coordinate free, high-resolution, point cloud segmentation of the surface (Fig. 2.1B).

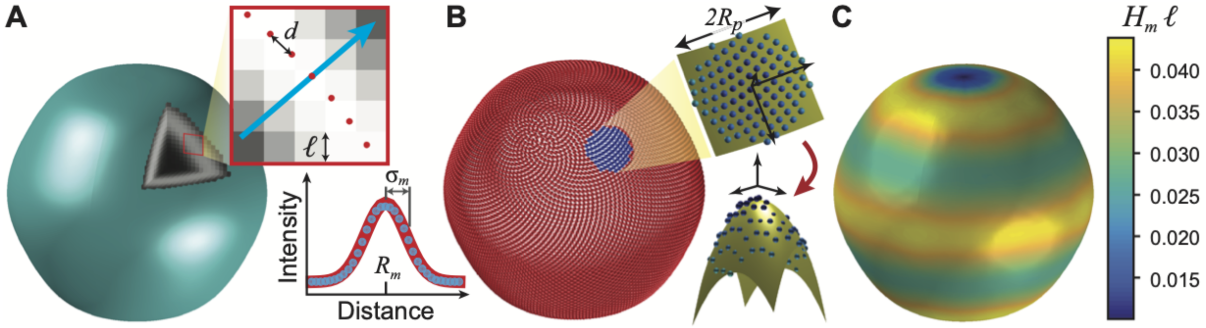

Figure 2.1: **Generation of the point cloud and measurement of local mean curvatures.** (A) Object to be reconstructed, featuring a cutaway displaying voxels along $x-$, $y-$ and $z-$planes. Upper right: Detail of $x$-plane section with the nearby reconstructed surface coordinates overlaid (red dots). Voxel length is $\ell$ and typical spacing between reconstructed points is $d$. For the case shown, $d = \ell$. The light blue arrow illustrates a segment along the local normal direction to the surface used to locate peaks in intensity. The intensity along the length of the segment (blue dots), as well as a gaussian fit to the intensity profile (continuous red line), are shown in the lower right panel. The measured center-to-surface distance $R_m$ and the interface width $\sigma_m$ are determined from a gaussian fit of this trace. (B) Reconstructed point cloud (red dots) representation of the surface, with an example of a patch of coordinates of radius $R_p$ (dark blue dots). A local reference frame for the patch is determined and a 2D second order polynomial is fitted (golden surface) to the reconstructed surface coordinates within the patch (lower right panel; vertical scale is exaggerated for clarity). (C) Surface map of measured mean curvatures $H_m$ obtained as described in the main text.

## 2.3 Measuring Curvature from the Point Cloud

Obtaining curvatures from ordered or coordinate free point clouds can be done in different ways [64, 70, 71, 72]. Using local derivatives leads to significant errors even after smoothing the data [70]. For this reason, and also because we are interested in developing a coordinate free method to analyze arbitrary shapes [73], we use local quadratic fits to the surface within a neighborhood (or patch) of every surface point [70, 60]. Performing a local quadratic fit is equivalent to performing an integral, providing higher precision in the calculation of local curvatures.

We define the patch around an arbitrary point $Q$ as the interior of a sphere with patch radius $R_p$ centered at Q, with all the points within a distance $R_p$ from $Q$ considered part of $Q$'s patch. For each patch, we calculate the eigenvectors of the local covariance matrix, which form a natural right-handed coordinate system ($x$, $y$, $z$) and define the local frame of the patch. We then fit a second order polynomial $z = f(x, y)$ to the points in that patch, where

$$f(x, y) = a_1x^2 + a_2xy + a_3y^2 + a_4x + a_5y + a_6 \tag{2.1}$$

and $z$ is the distance from the centroid of the patch along the eigenvector that characterizes the direction normal to the patch (Fig. 2.1B). The other dimensions, $x$ and $y$, are also measured from the patch's centroid. The mean and Gaussian curvatures, $H$ and $K$ respectively, at point $Q$ are obtained from the coefficients of the second order fit evaluated at the projection of $Q$ onto the fitted surface along $z$. In terms of the fitted polynomial $f(x, y)$, the mean and Gaussian curvatures read[74]

$$H = \frac{(1 + f_y^2)f_{xx} - 2f_xf_yf_{xy} + (1 + f_x^2)f_{yy}}{2(1 + f_x^2 + f_y^2)^{3/2}} \tag{2.2}$$

$$K = \frac{f_{xx}f_{yy} - f_{xy}^2}{(1 + f_x^2 + f_y^2)^2} \tag{2.3}$$

where $f_x = 2a_1x + a_2y + a_4$, $f_y = a_2x + 2a_3y + a_5$, $f_{xx} = 2a_1$, $f_{yy} = 2a_3$, and $f_{xy} = a_2$.

In order to calculate local curvatures on the surface, it is necessary to specify the patch size, $R_p$. Importantly, the precision in the calculation of the local curvature depends on the patch size: small patches contain very few points, whereas large patches may capture curvature variations along the surface rather than performing a local measurement. More specifically, if $R_p$ is too large, then a second order polynomial fit may not adequately capture the surface within the patch, leading to a larger error in the determination of the local curvature. Alternatively, given the finite precision of the point cloud, if $R_p$ is too small, the patch contains insufficient information to accurately assess the local shape of the object. The proper choice of $R_p$ depends on the local curvature and for this reason we develop an adaptive algorithm, as described below.

We first roughly estimate the patch size as $R_p = (2\ell/H_{\text{est}})^{1/2}$, where $\ell$ is the voxel size (Fig. 1A) and $H_{\text{est}}$ is an estimate of the mean curvature at $Q$ corresponding to the local mean curvature of the globally fitted ellipsoid at $Q$. To better adapt the patch size to the local geometry of the surface, we perform local surface fittings using a local patch size with this estimate for the local $R_p$. From these surface fittings we obtain the mean and Gaussian curvatures, which we then use to determine the principal curvatures $\kappa_1$ and $\kappa_2$, where

$$\kappa_1 = H + \sqrt{H^2 - K} \quad \text{and} \quad \kappa_2 = H - \sqrt{H^2 - K}\,. \tag{2.4}$$

To further adapt the patch size to the local surface geometry, we then estimate the new local patch size using the local value of the maximal principal curvature $\kappa_{\text{max}} = \max(\kappa_1, \kappa_2)$, namely $R_p = (2\ell/\kappa_{\text{max}})^{1/2}$. Note that this is the size of the patch for which the displacement of the surface along its normal direction becomes $\ell$. We ensure that the value of $R_p$ does not lead to too large or too small patches that would increase the error of the curvature measurement by imposing both a minimum patch radius and a maximum range of the mean curvature variation within the patch. We require $R_p$ to be larger than $(18/\pi)^{1/2}\ell$, so that there are, on average, at least 3 points for every fitting parameter. Moreover, if the measured mean curvatures within the patch change by a factor of two or more compared to the measured mean curvature $H_m$ at $Q$, $R_p$ is reduced until the variation is less than a factor of two, or until $R_p = (18/\pi)^{1/2}\ell$, whichever comes first. Once the new patch size has been determined for every point in the point cloud (each point may have a different patch size) using the adaptive method and rules defined above, we obtain the mean curvature from the second order polynomial fittings described above. To prevent high-frequency noise from derailing the adaptive algorithm upon successive iterations, we apply median filters to the radial coordinate of the point cloud and to the measured curvatures at each iteration.

The resulting data set from the procedure described above is a surface map of the mean curvature $H$ (Fig. 2.1C). Similar maps for the Gaussian curvature and principal curvatures can be obtained from the analysis, but we focus on the mean curvature below for simplicity.

## 2.4 Testing Accuracy with Model Objects

Many factors affect the accuracy of the segmentation and analysis of the surface geometry. We examine the effect of the object shape and size, as well as image noise and resolution, on the segmentation accuracy and the determination of surface mean curvatures of the algorithm presented above. To do so, we mathematically define an object, simulate a 3D fluorescence microscopy image of the object, and use the algorithm described above to reconstruct the object from the generated synthetic image data. The accuracy of the algorithm is quantified by comparing the measured center-to-surface distances, $R_m$, and mean curvatures, $H_m$, to their true values.

We considered shapes for which the inverse square of the radial coordinate can by expressed as a sum of $l =$ even, $m = 0$ terms in a spherical harmonic expansion, up to sixth order. These include a sphere, an ellipsoid, a fourth order shape, and a sixth order shape, defined by

$$r(\phi) = (AY_0^0 + BY_2^0(\phi) + CY_4^0(\phi) + DY_6^0(\phi))^{-1/2} \tag{2.5}$$

where

$$Y_l^0(\phi) = \sqrt{\frac{2l+1}{4\pi}} P_l(\cos\phi) \tag{2.6}$$

and $P_l(x)$ is the $l^{\text{th}}$ degree Legendre polynomial. The shape of the object is determined by the particular choice of coefficients $A$, $B$, $C$, and $D$ in Eq. 2.5. The size of the object is determined by the parameters chosen to simulate the synthetic image data, which include the pixel size, the step size in $z$, and the size of the point spread function (PSF). For simplicity, the pixel size and step size are both equal to $\ell$ and the PSF is modeled as a spherically symmetric Gaussian of width $\sigma_t$. The image stack is constructed by convolving the PSF with a set of points located on the analytical surface, a process analogous to imaging a closed object with fluorescent molecules located at its surface using 3D fluorescence microscopy (such as confocal microscopy). We used approximately two points per square pixel to generate these images and all intensity values in the array are scaled such that the maximum intensity is 128. The image is then saved as an 8-bit tiff stack. To encourage even simulated surface illumination the intensity of each point is weighted inversely to its local density, so that regions with higher local density of points generate approximately the same surface intensity as regions with lower densities.

We evaluated the accuracy of the algorithm's surface segmentation for four differently shaped objects of the same size (Fig. 2.2). To quantify the algorithm's error in detecting the location of the surface, we define the center-to-surface distance as $R$ and a measure of the relative error of $R$ as $\epsilon_R = (R_m - R_t)/R_0$, where $R_t$ are the true values of the center-to-surface distances and $R_0$ is the global average of $R_t$. In general, we observe that $\epsilon_R$ is largest in magnitude at local maxima of $R$ (Fig. 2.2B). For this reason, $\epsilon_R$ varies with elevation in objects in which $R$ also varies with elevation (Fig. 2.2B). These

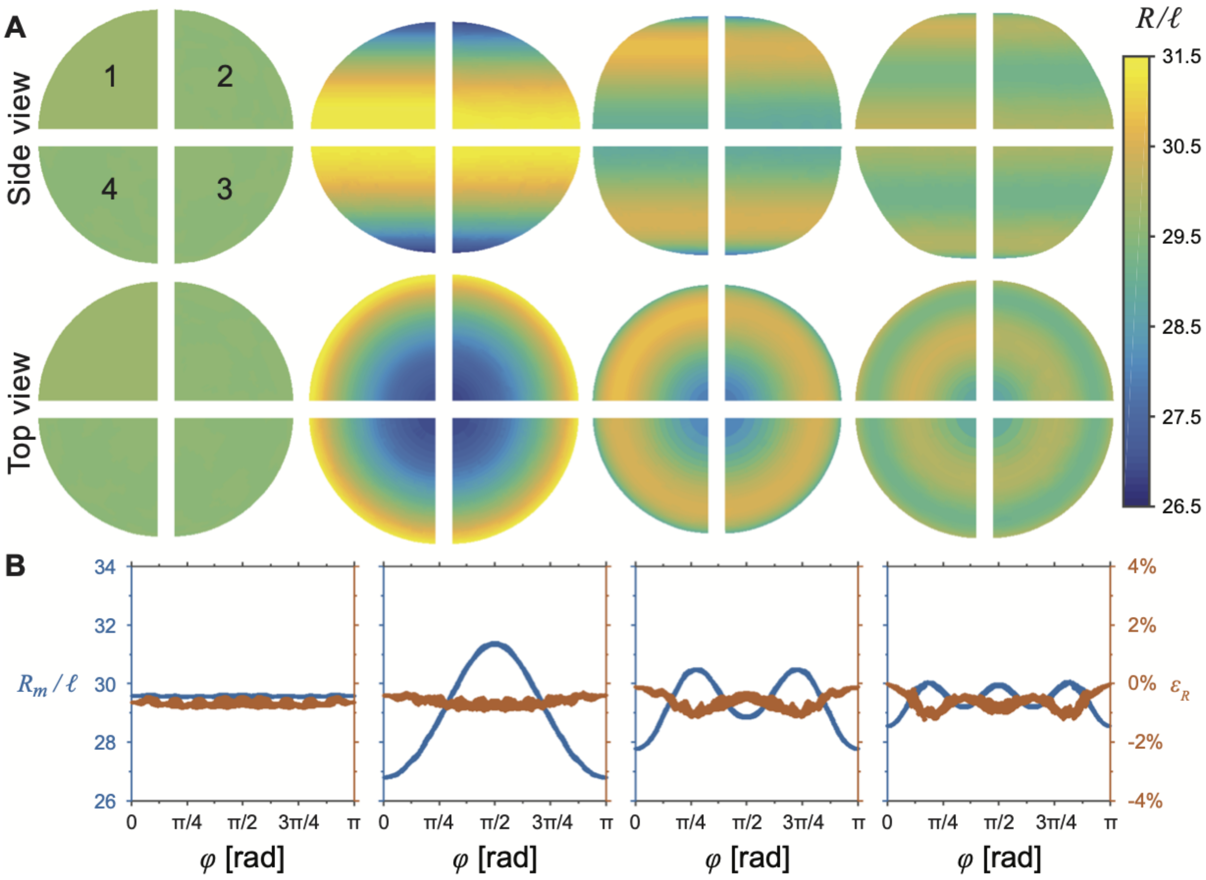

Figure 2.2: **Accuracy in the determination of the surface location.** (A) Side and top views of objects (from left to right: sphere, ellipsoid, 4th order shape, and 6th order shape), color coded with the radial distance from the object center. The different quadrants show the analytical surface (Quadrant 1), the reconstructed surface in the absence of noise (Quadrant 2), the reconstructed surface in the presence of 8.84 % shot noise (Quadrant 3) and the reconstructed surface in the presence of 5 % background noise (Quadrant 4). The parameters for constructing the objects are: sphere: $A\sigma_t^{1/2} = 0.016$, $B = 0$, $C = 0$, $D = 0$; ellipsoid: $A\sigma_t^{1/2} = 0.016$, $B/A = 0.1$, $C = 0$, $D = 0$; 4th order object: $A\sigma_t^{1/2} = 0.016$, $C/A = 0.05$, $B = 0$, $D = 0$; 6th order object: $A\sigma_t^{1/2} = 0.016$, $D/A = 0.025$, $B = 0$, $C = 0$. $\sigma_t/\ell = 2$ and $R_t/\ell$ spans 26.8 to 31.4. (B) Reconstructed surface position, $R_m$, and relative errors in the detection of the surface position, $\epsilon_R$, in the absence of noise. Vertical left (blue) and right (orange) axes show $R_m$ (normalized by $\ell$) and $\epsilon_R$ as a function of the zenith angle $\phi$.

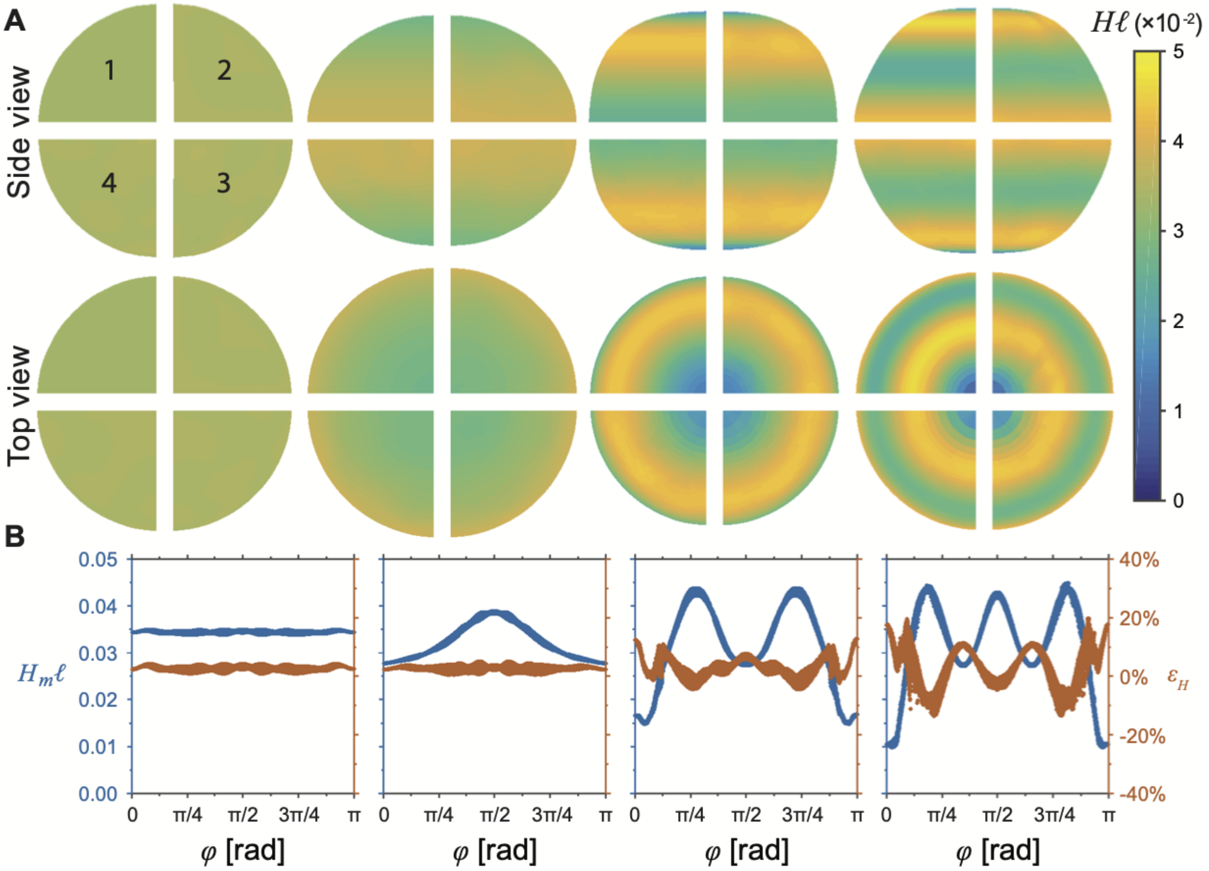

Figure 2.3: **Accuracy in the determination of local mean curvatures.** (A) Side and top views of objects (as described in Fig. ??A), color coded with the surface map of mean curvatures. Quadrants are as described in Fig. ??A. $H_t\ell$ spans 0.0046 to 0.046. (B) Reconstructed mean curvature, $H_m$, and relative errors in the detection of the mean curvature, $\epsilon_H$, in the absence of noise. Vertical left (blue) and right (orange) axes show $H_m$ (normalized by $\ell^{-1}$) and $\epsilon_H$ as a function of the zenith angle $\phi$.

errors are systemic and negative, meaning the center-to-surface distance is generally underestimated. In these objects, local maxima in $R$ are also local maxima in $H$. The observation that $\epsilon_R$ increases with $H$ can be explained by the asymmetry in the intensity profile which occurs at a curved interface, analogous to how the center of mass of a segment of a thin ring may lie inside the ring. Despite the small bias in the surface determination, this algorithm can detect the surface with sub-pixel resolution (absolute error less than $0.34\ell$) and the magnitude of $\epsilon_R$ is less than 1.24 % in the absence of noise for the objects considered (Fig. 2.2).

We also evaluated the accuracy of the algorithm in determining the local mean curvature for the four shapes described above (Fig. 2.3). We define the relative error of $H$ as $\epsilon_H = (H_m - H_t)/H_0$, where $H_m$ and $H_t$ are the measured and true values of the mean curvature, respectively, and $H_0$ is the global average of $H_t$. The error in the determination of the local curvature depends on the local geometry of the object. Regions with high mean curvature tend to have smaller relative errors than regions with low mean curvature (Fig. 2.3B). Moreover, in surface regions where the curvature varies considerably within the patch, the relative error of the curvature can also be significant. We observe that regions with low mean curvature display both higher relative and absolute errors in $H$. We believe this is because accurate measurements of the curvature can only be obtained if the surface inside the patch is reasonably approximated by its second order (quadratic) expansion. Given the finite resolution of our representation of the object (in the image and in the point cloud), it is not always possible to make the patch small enough for this approximation to be suitable. In such cases, we must accept that we are not able to discern the true curvature of an object's surface with limitless precision; rather, we are characterizing variations in shape which occurs above a certain length scale.

In most experimental situations, it is important to quantify the robustness of the algorithm when noise is present in the system and when images are obtained at different resolutions. To test such conditions, we simulated imaging of the sixth order shape from Figs. 2.2 and 2.3 at three different resolutions ($\sigma_t/\ell = 1$, $\sigma_t/\ell = 2$, $\sigma_t/\ell = 4$) and a range of noisy conditions (Fig. 2.4A). The simulated images are 8-bit and the maximum intensity $I_m$ in the raw (noise-free) images was set at $I_m = 128$. We consider both the effect of un-correlated and correlated noise sources in the intensity, which we call background and shot noises, respectively. Background noise, defined as an spatially uncorrelated noise in the intensity with magnitude following an exponential distribution, is added directly to the raw image volume. We report the level of background noise as the ratio of the average intensity of noise to the maximum intensity in the raw image. To simulate shot noise,

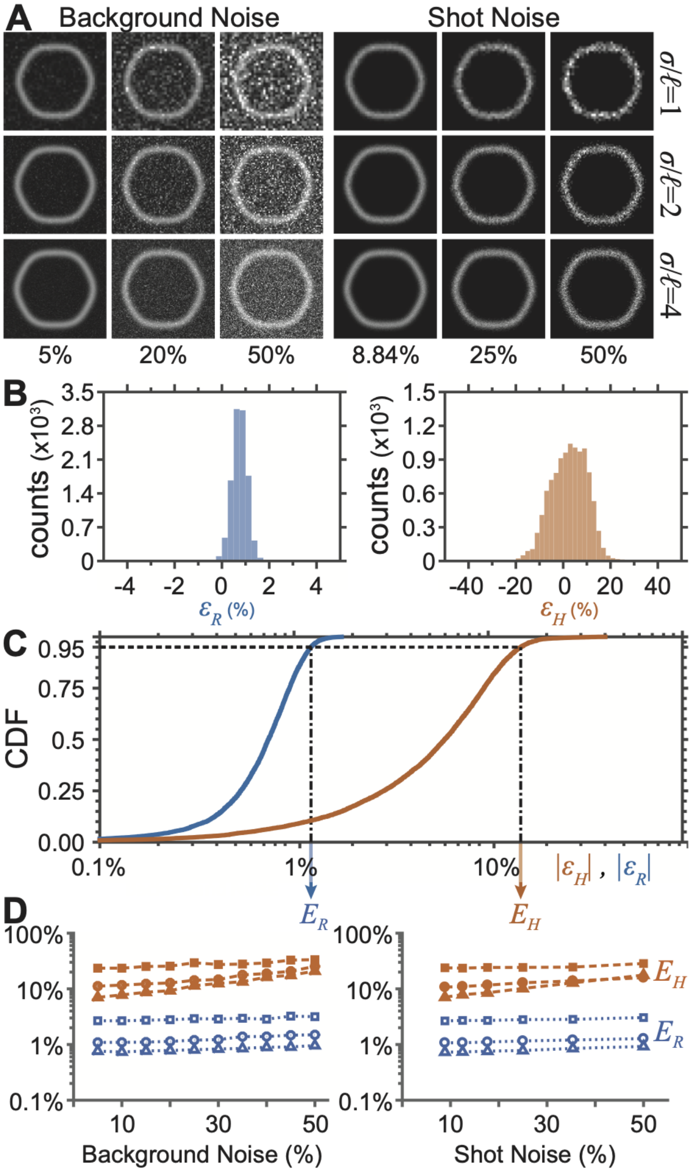

Figure 2.4: **Effect of image resolution and noise in surface segmentation and measurement of mean curvatures.** (A) Matrix of image sections through a 6th order shape showing the range of resolutions and noise (both background and shot noise) levels considered. (B) Example of frequency histograms of $\epsilon_R$ and $\epsilon_H$ for a reconstructed object. (C) Cumulative distribution functions (CDFs) for $\epsilon_R$ and $\epsilon_H$ illustrating the definition of error metrics $E_R$ and $E_H$. (D) Obtained values of $E_R$ (blue) and $E_H$ (orange) as a function of background and shot noise levels, for different imaging resolutions, namely $\sigma/\ell = 1, 2, 4$ (squares, circles, triangles, respectively).

the intensity in each voxel in the noisy image is drawn from a Poisson distribution with a mean proportional to the corresponding raw voxel intensity in the absence of noise. That is, if the raw intensity of a given voxel is $I_r$, we substitute the intensity value at this voxel by $I_n \equiv \alpha m$, where $m$ is a number drawn from a Poisson distribution with mean $I_r/\alpha$ and $\alpha$ is a positive real number analogous to a digital gain. The parameter $\alpha$ is introduced to study the effect of varying noise while keeping the average image intensity constant. With these definitions, the level of noise is given by $\sqrt{\alpha/I_m}$ (Fig. 4A).

In order to evaluate the quality of the reconstruction and characterization of a surface's mean curvature map in the presence of noise, we defined two scalar metrics, $E_R$ and $E_H$, for the error in $R$ and $H$, respectively. A given surface reconstruction is characterized by different relative errors at every point of the surface (Figs. 2 and 3). The probability distribution of the absolute values of $\epsilon_R$ and $\epsilon_H$ (Fig. 2.4B) allows us to calculate statistics of the errors on the surface. We define $E_R$ as the value of $|\epsilon_R|$ for which its cumulative distribution function (CDF) is 0.95 (Fig. 2.4C), such that 95% of the relative errors $|\epsilon_R|$ are smaller than $E_R$. Similarly, $E_H$ is the value of $|\epsilon_H|$ for which its cumulative distribution function (CDF) is 0.95 (Fig. 2.4C), such that 95% of the relative errors $|\epsilon_H|$ are smaller than $E_H$. For almost all noise levels investigated here, increasing resolution led to smaller errors in both the segmentation and curvature measurements. It was also observed that increasing the noise level increased the error in the segmentation and curvature measurements, though the effect is moderate even for relatively large noise levels (Fig. 2.4D). Due to the pre-processing of the images with median filtering, and the nature of the segmentation by 1D fitting and curvature analysis by 2D fitting, we can detect the surface with very high precision even with substantial amount of noise (relative errors below 3 % even at 50 % noise levels; Fig. 2.4A,D) and we can obtain the mean curvature with good precision even for levels of noise that considerably affect the image (relative errors below 30 % even at 50 % noise levels; Fig. 2.4A,D). Our results indicate that improving image resolution has a stronger effect in reducing both the segmentation error and the error in the determination of the curvature than reducing the noise in the images.

## 2.5 Analysis of Experimental Data

After having characterized the performance of the algorithm with controlled, synthetic data, we tested its performance with experimental data. To do so, we first used fluorocarbon oil droplets with fluorescently-labeled surfaces, as previously described [5, 75]. Droplets were generated and coated as described in [75] and mixed with an aqueous solution containing low-melting point agarose at 1 % (v/v). Temperature was lowered below the gelation point, immobilizing the droplets in the agarose gel. The droplet radii (9-11$\mu$m) were well below the capillary length for these droplets ($569 \pm 5$ microns in water, $543 \pm 5$ microns in cell culture media) and, therefore, gravity did not significantly deform the droplets from a pure spherical shape. The spherical droplets were imaged using a laser scanning confocal microscope (Zeiss LSM 710, Zeiss Inc.) at various laser powers with a resolution of $\ell_x = \ell_y = 0.42\,\mu$m and step size in $z$ of $\ell_z = 1\,\mu$m. We reconstructed the droplets using the algorithm described above (Fig. 2.5A-D) and quantified the error in the reconstructions (Fig. 2.5E-F). For a spherical droplet, the average droplet radius can be approximated by the global average over the droplet surface of the measured radius $R_m$, which we define as $R_0$. Similarly, we define $H_0$ as the global average over the droplet surface of the measured mean curvature, $H_m$. These definitions allow the calculation of the relative errors $\epsilon_R$ and $\epsilon_H$ in the $R$ and $H$, respectively, as well as $E_R$ and $E_H$, as defined above. The average values of $E_R$ and $E_H$ obtained for multiple droplets ($N = 5$) of different radii were 0.88 % and 7.9 %, respectively. The errors for the smallest drop ($R_0/\ell_x = 22.1$) are shown in Fig. 2.5C,D. The measured values of both error measures,

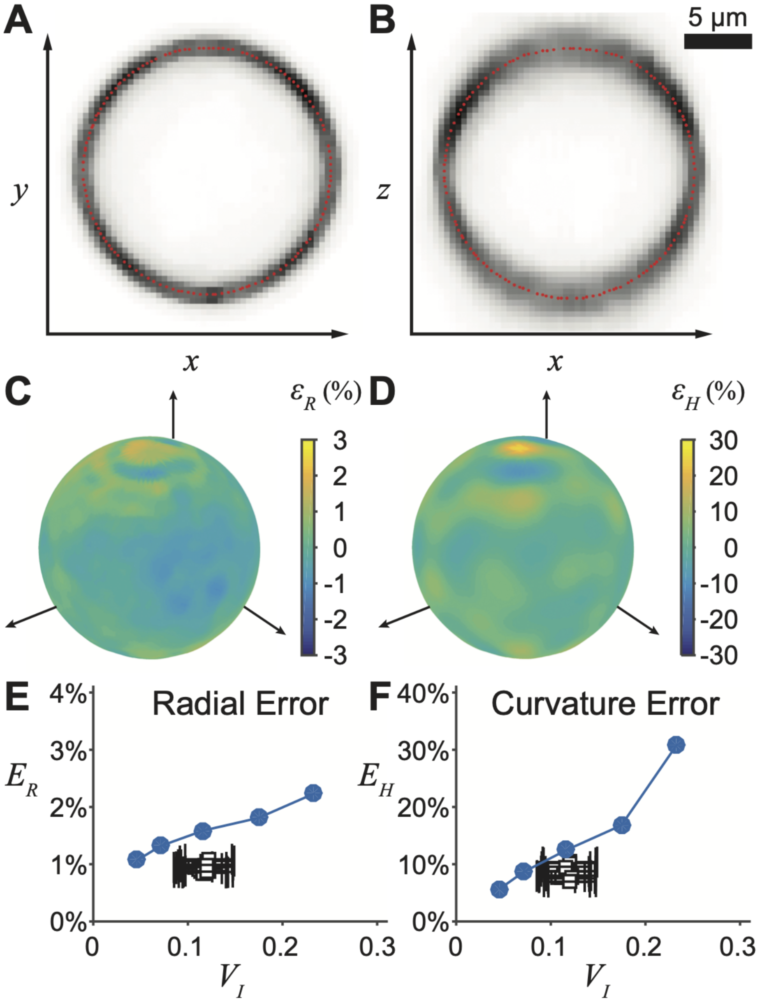

Figure 2.5: **Reconstruction of spherical droplets with a surface fluorescent label.** (A-B) $x - y$ (A) and $x - z$ (B) sections from a confocal image stack (inverted) of a spherical droplet in 1 % agarose gel ($R_0/\ell_x = 22.1$, $\ell_x = 0.42\,\mu$m, $\ell_z = 1\,\mu$m), after median filtering and with reconstructed coordinates overlaid (red dots). (C-D) Reconstructed droplet shape displaying the estimated error in the radial coordinate $\epsilon_R$ (C) and in the mean curvature $\epsilon_H$ (D). (E-F) Measured values of $E_R$ (E) and $E_H$ (F) as a function of $V_I$ for a droplet imaged at different laser powers (black squares). Error bars correspond to the standard deviation. Values of $E_R$ (E; blue circles) and $E_H$ (F; blue circles) as a function of $V_I$ for a spherical object ($R_t/\ell = 22, \sigma_t/\ell = 1.4$) simulated at levels of noise similar to those observed experimentally (different levels of shot noise are shown; constant background noise of 0.62%).

$E_R$ and $E_H$, for all measurements of the $R_0/\ell_x = 22.1$ droplet were then compared to the errors values from a simulated spherical droplet ($R_t/\ell_x = 22$, $\sigma_t/\ell_x = 1.4$) and noise levels as those measured experimentally (Fig. 2.5E-F). In order to compare simulated droplets with experimental droplets, we define the coefficient of variation of the surface intensities, $V_I$, as the average over all the z-planes of the ratio of the standard deviation and average of surface pixel intensities in each z-plane. Since $V_I$ provides information about the relative variation of the surface intensities, we use it as a proxy metric for shot noise. Despite the additional potential sources of noise in the experiments, the values of $E_R$ and $E_H$ for experimental and simulated (synthetic) droplets are in good agreement (Fig. 2.5E-F) for similar values of $V_I$, indicating that the use of synthetic data provides reasonable estimates of the errors in segmentation and curvature measurements.

After having established that the developed algorithm is able to provide accurate segmentation and curvature maps of surfaces, we use it to characterize the geometry of oil droplets deformed by cellular forces. Fluorocarbon oil droplets similar in size to individual cells, coated with ligands (RGD) targeting integrin receptors, were generated as recently reported [75, 5]. These droplets were injected in multicellular aggregates of tooth mesenchymal cells and subsequently imaged using previously described protocols [5]. Once inside the cellular aggregate, droplets were deformed by compressive and tensile stresses generated by the cells. The droplet deformations, and specially the mean curvatures of the droplet surface (mean curvature map), have been shown to provide a direct readout of cell-generated mechanical stresses [5]. Using the algorithm described above, we segmented the surface of the droplets and determined the mean curvature map. An example of the droplet segmentation and measured mean curvatures is shown in Fig. 2.6. While it is impossible to obtain a true value of the error in the segmentation and mean curvatures for these droplets, as their true shape in unknown (in contrast to the data generated synthetically above), we estimate it as follows. For a given droplet,

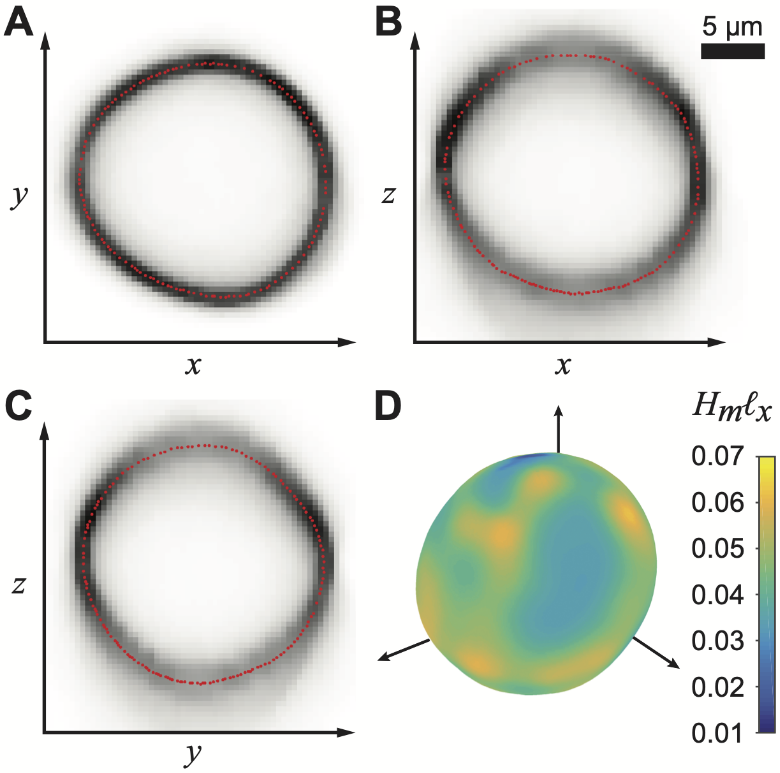

Figure 2.6: **Reconstruction of a droplet with a surface fluorescent label, deformed by cellular forces inside a multicellular aggregate.** (A-C) $x-y$ (A), $x-z$ (B) and $y-z$ (C) sections from a confocal image stack (inverted) of a droplet ($R_0/\ell_x = 23.0$, $\ell_x = 0.42\,\mu$m, $\ell_z = 1\,\mu$m) embedded in a mesenchymal cell aggregate and deformed by cellular forces, after median filtering, with reconstructed coordinates overlaid (red dots). (D) Reconstructed droplet shape displaying the measured values of mean curvatures $H_m$ (normalized by $\ell_x^{-1}$) at the droplet surface.

we obtain the value of $V_I$ and estimate the error by simulating a spherical droplet with similar resolution and noise. For the specific case of the droplet shown in Fig. 2.6, $V_I = 0.10 \pm 0.03$ (mean ± std) and we estimate the segmentation error and the error in determination of the mean curvature to be $E_R = 1.6\%$ and $E_H = 12.5\%$. While it is impossible to determine if this is the actual error as the real droplet shape is unknown, we believe it provides a reasonable estimate of the accuracy of the reconstruction given the good agreement between simulated and measured errors described above (Fig. 2.5).

## 2.6 Conclusions

We have developed a fully automated algorithm to segment fluorescently-labeled surfaces obtained from 3D fluorescence microscopy (confocal, multiphoton or light-sheet imaging) and characterize their geometry. We thoroughly characterize the ability of the algorithm to perform accurate surface segmentation and local mean curvature measurements using both synthetic data and experimental spheres (droplets). Finally, we use the algorithm to reconstruct oil droplets embedded in multicellular aggregates and deformed by cellular forces.

Our results indicate that the algorithm can detect the location of fluorescently-labeled surfaces with sub-pixel resolution, and relative errors below 2% for typical imaging conditions and even in the presence of substantial noise. The ability to segment surfaces at high resolution can be used in many studies, from soft-matter physics to biology. Regarding the characterization of surface geometry, the presented algorithm can obtain the mean curvature at each point of the surface with high enough accuracy (typically better than 20%) to perform quantitative measurements, even in the presence of substantial noise. We find that improving the image resolution, rather than reducing image noise, leads to lower errors in both segmentation and mean curvature measurements.

However, the use of raytracing to segment with high resolution carries some limitations. Objects with spherical topology but with very large surface deformations leading to rays crossing the object's surface multiple times cannot be reconstructed using this algorithm. Similarly, extreme noise levels can generate multiple intensity maxima along the rays, hindering the ability to properly reconstruct the surface of the object. Beyond limitations associated with raytracing, in its present form this algorithm does analyze objects with a fluorescently-labeled surface but not objects labeled in their bulk. This limitation may easily be overcome by fitting functions other than Gaussians (e.g., hyperbolic tangent) to determine the location of the interface along the ray. Finally, this algorithm does not have the ability to automatically isolate an object of interest if multiple objects are present in the image volume. Manual cropping of the object of interest is required. Analysis pipelines could be developed to automatically isolate multiple objects in the original image for independent analysis with the presented algorithm.

We believe this method will enable researchers in different research disciplines to measure variations in surface curvature of microscopic objects such as cells, emulsion droplets, vesicles, etc., in a quantitative manner. The source code of the algorithm can be downloaded at
https://github.com/ElijahShelton/drop-recon.

## 2.7 Permissions and Attributions

1. The content of chapter 2 is the result of a collaboration with Friedhelm Serwane and Otger Campàs, and has previously appeared in the Journal of Microscopy [1]. It is reproduced here in accordance with rights retained by the authors. To find the work as it originally appeared: `https://doi.org/10.1111/jmi.12624`.

---

[1] E Shelton, F Serwane, O Campàs. Geometrical characterization of fluorescently labelled surfaces from noisy 3d microscopy data. *Journal of Microscopy* 269 (3), 259-268 (2018)

# Chapter 3

# Mechanical stresses guiding body axis elongation in zebrafish

## 3.1 Introduction

The formation of an animal's anterior to posterior (AP) body axis is a critical step in establishing an individual's body plan. In vertebrates, the posterior elongation of the body is coordinated with axial segmentation (a.k.a. somite formation) to determine the overall length of the animal, and generate the exact number of segments particular to a given species. While the cellular behaviors involved in axis elongation have been well studied, and many of the genetic signaling pathways involved have been identified, the physical mechanisms underlying body axis elongations have not been characterized [6].

The vertebrate body is built from head to tail (anterior to posterior). To supply material to the extending body, cells from the dorsal aspect enter a region in the posterior-most end of the "tailbud" called the mesodermal progenitor zone (MPZ). These cells are eventually incorporated into the presomitic mesoderm (PSM), and ultimately section off from the PSM when they form somites. This process of growth is sustained until the entire length of the body axis is established. While it is generally understood that cellular and tissue movements arise, ultimately, from the generation of physical stresses (forces per unit area), a quantification of these forces has, prior to the work presented here, been nonexistent. In this chapter, I present the first quantitative measurements of forces in any embryonic process.

how stresses are patterned along the AP body axis have so far been lacking in any embryonic process.

## 3.2 Results

In order to quantify how stresses are patterned along the AP axis, we first defined different regions: the medial-MPZ (M-MPZ), the lateral-MPZ (L-MPZ), the posterior-PSM (P-PSM), and the anterior-PSM(A-PSM)(Fig. 3.1a-b). By injecting magnetically responsive oil droplets (Methods), we made a series of stress measurements in different regions along the AP axis (Fig. 3.1c). In the absence of an applied magnetic field, the shape of the oil droplets is determined by endogenous stresses present in the tissue[5]. To measure tissue-scale stress, we quantified the amplitude of stress anisotropies associated with the ellipsoidal mode of the droplet by fitting an ellipse to the imaged section of the droplet (Fig. 3.1d; Methods). We found that supracellular or tissue-scale stresses are greatest at the anterior and decrease towards the posterior end (Fig. 3.1e). The orientation of the stress anisotropy is also regionally variant, as droplet orientations in the PSM exhibit a bias towards alignment with the AP axis while drops in the M-MPZ were more likely to be oriented along the ML axis (Fig. 3.1f). The amplitudes of the ellipsoidal strain persists in the PSM and MPZ over periods greater than 30 minutes (Fig. 3.1g), a relevant developmental timescale set by the period of somitogenesis in zebrafish at 25°C[76].

We were also interested in stress inhomogeneities at the cellular scale. To quantify the amplitude of cellular stresses, I first measured local curvatures along the droplet boundary (Fig. 3.1h; methods), and then quantified the deviation in local curvature from the curvature of the fitted ellipse (Fig. 3.1d; methods). Using the measured values of interfacial tension (methods), I related amplitudes of deviations in local curvature to amplitudes of cell scale stresses with two metrics: the average cell-scale stress, and the maximum cell-scale stress (Fig. 3.1i; methods). Neither measure of cell-scale stress showed spatial variation along the AP axis. To confirm that the local stresses variations I was quantifying were indeed cell-scale, I compared the characteristic lengths of local curvature variations to measurements of cell diameter (Fig. 3.1j). To understand the dynamics of cell-scale stresses, I performed temporal autocorrelation on local curvature time traces from 4 different droplets (Fig. 3.1k), methods). This showed cell-scale stresses to be temporally short-lived, with a half-life on the order of 1 minute, comparable to the timescale associated with correlation of cell-cell junction length fluctuations [77].

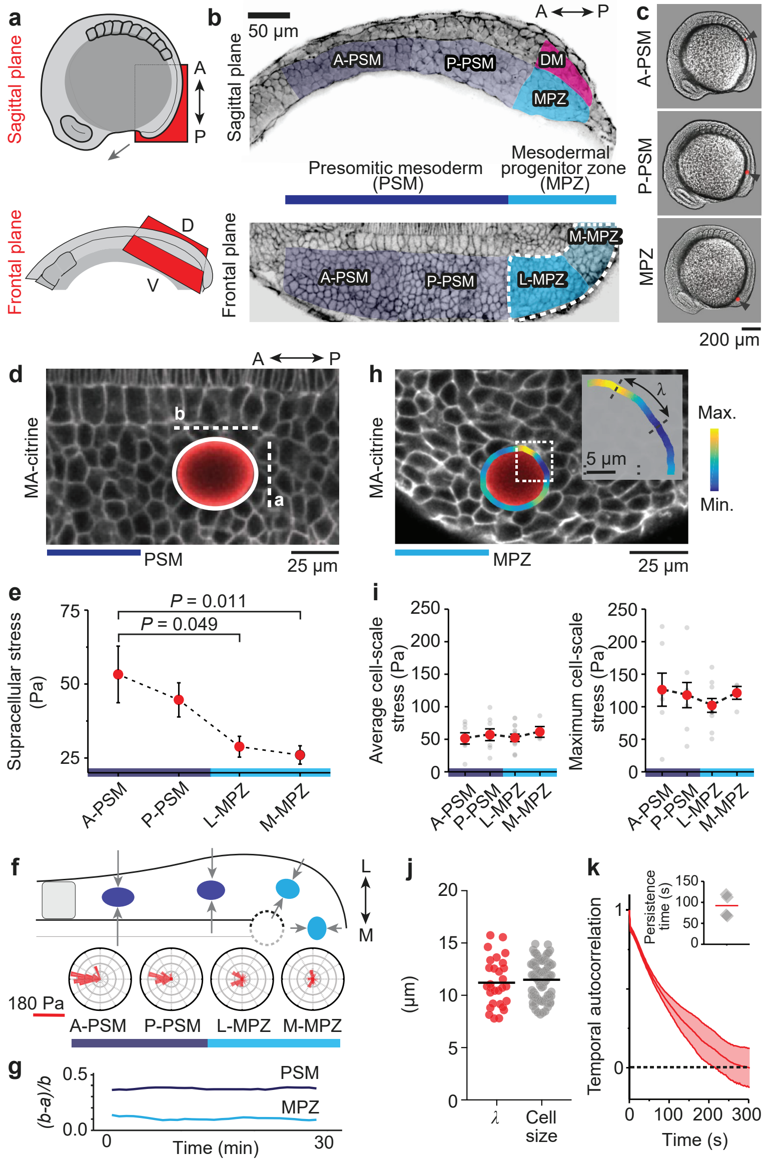

Figure 3.1: **Supracellular and cell-scale mechanical stresses during body axis elongation.** (A) Sketch showing lateral views of a 10-somite stage embryo and sagittal and frontal anatomical planes. A, anterior; P, posterior; V, ventral; D, dorsal. (B) Confocal sections along sagittal and frontal planes of posterior extending tissues in Tg(actb2:MA-citrine) embryos (inverted). The PSM is divided into anterior (A-PSM) and posterior (P-PSM) regions and the MPZ is divided into lateral (L-MPZ) and medial (M-MPZ) regions. The dorsal medial (DM) zone is dorsal to the MPZ. (C) Embryos with droplets (red; arrows) located in the different regions.

Figure 3.1: (D) Elliptical fit (white; $b$ and $a$ being the long and short semi-axes) of a ferrofluid oil droplet (red) in the PSM of a Tg(actb2:MA-citrine) zebrafish embryo (no magnetic actuation). (E) Magnitude of supracellular stresses along the anteroposterior axis (n = 9 (A-PSM), 24 (P-PSM), 25 (L-MPZ), 27 (M-MPZ); mean ± s.e.m.). Mann-Whitney U-test. (F) Bottom, orientation of the long axis of the droplets with respect to the anteroposterior axis (n = 15 (A-PSM), 12 (P-PSM), 11 (L-MPZ), 13 (M-MPZ)). M, medial; L, lateral. Top, sketch showing the average droplet orientations along the anteroposterior axis and the posterior-to-anterior increase in mediolateral constriction (arrows) in the PSM. (G) Time evolution of the ellipsoidal droplet deformation, $(b-a)/b$.(H) Ferrofluid droplet (red) in the MPZ of a Tg(actb2:MA-citrine) embryo. Inset, curvature values along the detected droplet contour (colour coded), with $\lambda$ being the distance between consecutive curvature maxima and minima. (I) Measured average (left) and maximal (right) cell-scale stresses along the anteroposterior axis (n = 7 (A-PSM), 8 (P-PSM), 10 (L-MPZ), 4 (M-MPZ); mean $\lambda$ s.e.m.). (J) Measured values of $\lambda$ (n = 29) and cell size (n = 100 cells). Line indicates mean. (K) Temporal autocorrelation of droplet shape deviations from the ellipsoidal mode (n = 2,062 curvature time traces obtained from 4 embryos). Average half-life is approximately 1 min (inset; n = 4; line indicates mean). Unless stated otherwise, n represents number of embryos.

## 3.3 Discussion

The spatiotemporal characterization of cell and tissue-scale stresses presented in this chapter contributed in the development of a physical model of body axis elongation, as described in publication [77]. To appreciate this physical model, I will briefly discuss the other major findings in Mongera, *et al*, 2018.

It was shown, through magnetic droplet experiments, that tissue in the PSM and MPZ behave as a yield stress material. Further, it was shown that the yield stress is spatially graded, being least in the MPZ and greatest in the A-PSM, proving the existence of a transition between fluid and solid tissue states. The demonstration that the growing posterior end of the body (the MPZ) maintains a fluid-like state provides an explanation for how new material is incorporated from the dorsal tissue, while the relatively solid-like PSM provides a rigid form upon which to build the posteriorly extending tissue. The spatial gradient in yield stress is explained in large part by measurements of an opposing gradient in volume fraction of extracellular space, according to predictions from an aqueous foam model. In *cdh2*$^{-/-}$ embryos, neither yield stress nor volume fraction showed any significant regional variation.

In addition to variations yield stress, regional variations were also observed in the amplitude of cell-cell junction length fluctuations as well as in the mean squared relative displacement (MSRD) of cell nuclei. In wild-type embryos, higher junctional fluctuation amplitudes were observed in the MPZ versus in the PSM. Under blebbistatin treatment, cell-cell junction fluctuations in the MPZ decreased in amplitude while the yield stress values in the MPZ increased, suggesting that cell junction fluctuations play a role in fluidizing the tissue in the MPZ. MSRD measurements were higher for cells in the MPZ versus the PSM, and indicated that uncaged movement occurs within a 30 minute time window in the MPZ. Together, these measurements suggest fluctuating, short-lived, cell-scale forces play role in maintaining a fluid-like state in the MPZ.

Considering these measurements together supports the hypothesis that embryonic tissues maintains a regional difference in rigidity/fluidity between the MPZ and PSM by tuning different parameters (volume fraction, active fluctuations, and supracellular stresses) within a jamming phase diagram. As cells from the MPZ mature to form the PSM, the cellular stresses persist at the same amplitude, playing a critical role in positioning the material state of the tissue near the jamming transition boundary. In this was increasing supracellular stresses in the PSM are sufficiently counteracted by decreasing extracellular volume fraction such that the system enters a jammed state within the PSM.

## 3.4 Methods

### 3.4.1 Zebrafish husbandry and fish lines

Zebrafish lines were maintained according to standard protocols [78] and all aspects of raising and experimentation were performed in accordance with protocols approved by the Institutional Animal Care and Use Committee (IACUC) at UC Santa Barbara. Tg(*actb2*:MA-citrine) embryos [79, 80] were used to provide labeling of cell boundary in the images used in this chapter. See publication [77] for details related to other fish lines used in the larger project.

### 3.4.2 Generation and injection of ferrofluid droplets.

Magnetically responsive, fluorescently labelled oil was prepared as described previously [81]. Briefly, DFF1 (Ferrortec) was diluted in fluorocarbon oil Novec 7300 (3M) to a concentration required to generate sufficiently large deformations in the tissue under the application of an applied magnetic field. Krytox-PEG(600) surfactant (0080-fluorosurfactant, RAN Biotechnologies [82]) was diluted to a weight percentage of 2.5%. Custom synthesized fluorinated rhodamine dye [83] was added to a concentration of 37µM. To allow for an accurate mapping from applied magnetic field to applied stress within the tissue, a calibration of the magnetic oil dilution was performed as previously described [81]. Droplets were formed by direct pneumatic injection into the targeted tissue, also as previously described [81]. Droplets were injected into tissue at 4-somite stage for measurements in the PSM and at the 6-somite stage for measurements in the MPZ. Tissue was allowed to recover for at least 2 hours after injection prior to imaging.

### 3.4.3 Mounting and imaging of zebrafish embryos.

Zebrafish embryos were mounted in 0.8% low-melting agarose at imaged at 25°C using a laser scanning confocal (LSM 710, Carl Zeiss Inc.). Images were acquired at 2.5 second intervals for droplet actuation experiments using a 40× water immersion objective (LD C-Apochromat 1.1 W, Carl Zeiss) or a 10× air objective (EC Epiplan-Neofluar 0.25, Carl Zeiss). Droplets were visualized using the fluorescent rhodamine dye. Zebrafish cell membranes were visualized via transgenic fluorescent labelling.

### 3.4.4 Measurement of tissue-scale stresses.

To quantify supracelular stresses, we measured the droplet ellipsoidal deformation, as this deformation mode reveals mechanical stresses that occur at the length scale of the droplet diameter (and slightly larger scales), which we purposefully made larger than the cell size (Fig.3.1d; droplet diameter: 44 ± 6 µm; cell diameter 11 ± 5 µm.; mean ± s.e.m.). We used ferrofluid droplets because their interfacial tension can be calibrated *in vivo* [81]. No magnetic field was applied on the droplet before or during the measurement of the supracellular stresses. Moreover, we prevented cell adhesion to the droplets to reveal the stresses associated soley with (supracellular) morphogenetic flows, mirroring previous studies in inert fluids[84]. Two hours after injection, the droplet was imaged mid-plane using confocal microscopy (LSM 710, Carl Zeiss Inc.). To quantify the ellipsoidal deformation of the droplet (and neglect high order deformations), we fitted an ellipse to the measured droplet shape, as previously described [81]. The value of anisotropic stresses for the ellipsoidal droplet deformation is given by $\sigma_T^A = 2\gamma(H_b - H_a)$, where $H_a$ and $H_b$ are the mean curvatures of the droplet at the intersection of the two principal axes with the ellipsoid and $\gamma$ is the droplet's interfacial tension (Fig.3.1d), as previously established [5, 85]. The mean curvatures $H_b$ and $H_a$ are given by $H_b = b/a^2$

and $H_a = 1/(2a) + a/(2b^2)$, $b$ and $a$ being the long and short semi-axis of the of the fitted ellipse, respectively (Fig.3.1d). At the end of each experiment, that is, after the recording of the shape of each droplet, we measured its interfacial tension $\gamma$ *in situ*, within the developing embryo, as previously described[81].

To obtain the direction of droplet deformation, we measured the angle between the direction defined by the long axis of the elliptical droplet deformation and the antero-posterior axis of the embryo using ImageJ[1].

While droplets cannot measure isotropic stresses because of droplet incompressibility[5], the ellipsoidal droplet deformation provides a quantitative measure of the difference in stresses along the direction of droplet elongation and perpendicular direction in the observation plane (the principal directions of the deformation). Ellipsoidal droplet deformations can, in general, be caused both by shear stresses or by stress differences along principal axes of droplet deformation (stress anisotropy).

### 3.4.5 Droplet shape segmentation and measuremen of in-plane curvature.

Confocal sections through the middle of a ferrofluid droplet were obtained by confocal microscopy, as described above. We then used a custom-made MATLAB code (adapted from a previously published code[85]) to obtain the coordinates of the droplet contour (segmentation) and measure the in-plane curvature $\kappa(s)$ along the droplet contour, with $s$ being the arc length along the contour. We first applied a Gaussian low-pass filter on the original raw image. The drop shape was identified from the filtered image using active contour segmentation to generate a mask. The edge was located by convolving the mask with the Sobel operator. The locations of edge pixels were then converted to ordered polar coordinates, which were smoothed using a moving average filter with a span of 5 pixels. We resampled the coordinates at even spacing using shape-preserving piecewise cubic interpolation. The curvature $\kappa(s)$ along the droplet contour was obtained by cubic fitting of edge coordinates over a small neighborhood of each point along the contour.

---

[1] This analysis was performed by Alessandro Mongera

### 3.4.6 Measurement of cell-scale stresses

To measure cell-scale stresses, or stresses associated with deformation modes of higher order than the ellipsoidal deformation mode (droplet deformations at length scales smaller than the droplet size), we used a similar procedure to the one described[5] to obtain cellular stresses from 2D confocal sections. Maximal and minimal values of the curvature along the droplet contour were spaced on average by the measured cell size (Fig. 3.1h,j), confirming that these deformations are associated with spatial variations in stresses occuring at the cell scale. In brief, we first segmented the 2D droplet shape and obtained the in-plane curvature $\kappa(s)$ along the droplet contour, as described above. We then calculated the deviations $\delta\kappa(s) \equiv \kappa(s) - \kappa_e(s)$ of the curvature along the contour from the curvature $\kappa_e$ of the elliptical deformation mode. We fitted an ellipse to the contour coordinates using the MATLAB function EllipseDirectFit(written by N. Chernov based on a previous algorithm) to determine the elliptical curvature $\kappa_e$, and then calculated directly $\delta\kappa(s)$ along the droplet contour. We then detected the maxima and minima of $\delta\kappa$ along the contour and defined the amplitude of curvature deviations from the elliptical mode as the difference between a consecutive maximum and minimum of curvature, $\delta\kappa^{\mathrm{max}}$ and $\delta\kappa^{\mathrm{min}}$, respectively, along the droplet contour, namely $\Delta\kappa_{\mathrm{C}} \equiv \delta\kappa^{\mathrm{max}} - \delta\kappa^{\mathrm{min}}$. We also defined the maximum amplitude of curvature deviations from the elliptical deformation mode, $\Delta\kappa_{\mathrm{C}}^{\mathrm{max}} \equiv \delta\kappa^{\mathrm{absmax}} - \delta\kappa^{\mathrm{absmin}}$, where $\delta\kappa^{\mathrm{absmax}}$ and $\delta\kappa^{\mathrm{absmin}}$ correspond to the absolute maximum and absolute minimum in $\delta\kappa$ along the droplet contour. The average and maximal values of the stresses associated to cell-sized deviations from the ellipsoidal mode, $\sigma_{\mathrm{C}}^{\mathrm{average}}$ and $\sigma_{\mathrm{C}}^{\mathrm{max}}$ respectively, are given by $\sigma_C^{average} = \langle 2\gamma\Delta\kappa_{\mathrm{C}}\rangle$ (average, indicated by the angled brackets, was calculated over multiple consecutive maxima and minima for a single droplet and also over multiple droplets in the same region of the tissue in different embryos) and $\sigma_{\mathrm{C}}^{\mathrm{max}} \equiv \langle 2\gamma\Delta\kappa_{\mathrm{C}}^{\mathrm{max}}\rangle$ (average was done over multiple droplets in the same region of the tissue in different embryos). As previously noted [5], this calculation assumes no major structural anisotropies in the tissue.

### 3.4.7 Length scale analysis of cellular stresses.

To measure the length scale associated with shape deviations from the elliptical deformation mode, we obtained the locations of maxima and minima of $\delta\kappa(s)$ along a droplet's contour, and calculated the contour distance $\lambda$ between consecutive maxima and minima (Fig. 3.1h).

### 3.4.8 Measurement of persistence in tissue-scale stresses.

To quantify the persistence timescale of tissue-level stresses, we imaged equatorial sections of magnetic droplets (no applied magnetic fields, as described above) at time intervals of one second for up to 30 minutes. We fitted ellipses to droplet sections at each time point and reported the droplet aspect ratio as a function of time. We observed no substantial change in the average droplet aspect ratio over the course of 30 minutes, indicating that tissue-level stress anisotropies persist in the tissue for longer than at least 30 minutes.

### 3.4.9 Measurement of persistence in cell-scale stresses.

To obtain the persistence of cell-scale stresses, we performed time-lapse imaging of ferrofluid droplets (no magnetic actuation) inserted in the MPZ tissue at 2.5-s time intervals, for 10 to 16 minutes. We segmented those droplets at each timepoint and obtained the in-plane curvature $\kappa(s,t)$ along the contour (parameterized with the contour length $s$), as well as the curvature deviations from the elliptical droplet deformation, $\delta\kappa(s,t)$, as described above. For each time-lapse, we resampled $\delta\kappa(s,t)$ at equal angular ($\theta$) spacing, to obtain $\delta\kappa(\theta,t)$. We then calculated the temporal autocorrelation $C_{\delta\kappa}(\tau)$, namely

$$C_{\delta\kappa}(\tau) \equiv \frac{\left\langle \left(\delta\kappa(\theta,t+\tau) - \langle\delta\kappa(\theta,t+\tau)\rangle_{\theta,t}\right)\left(\delta\kappa(\theta,t) - \langle\delta\kappa(\theta,t)\rangle_{\theta,t}\right)\right\rangle_{\theta,t}}{\sqrt{\left\langle \left(\delta\kappa(\theta,t+\tau) - \langle\delta\kappa(\theta,t+\tau)\rangle_{\theta,t}\right)^2\right\rangle_{\theta,t}}\sqrt{\left\langle \left(\delta\kappa(\theta,t) - \langle\delta\kappa(\theta,t)\rangle_{\theta,t}\right)^2\right\rangle_{\theta,t}}} \tag{3.1}$$

We reported $\tau_{1/2}$ for which $C_{\delta\kappa}(\tau)$ drops below 0.5 ($C_{\delta\kappa}(\tau_{1/2}) = 0.5$), which corresponds to its half-life and provides a measure of the timescale of correlation loss or, equivalently, the persistence timescale of cell-scale droplet deformations.

### 3.4.10 Measurement of droplet interfacial tension.

Droplet interfacial tension was determined by magnetic actuation as described previously [81], after imaging for stress measurements had been performed [77]. Briefly, under the application of a uniform magnetic field, the droplet is uniaxially deformed by an induced magnetic stress. The maximal strain achieved by the droplet is the result of stress balance between capillary forces and the magnetic forces. In this way, the interfacial tension can be determined from the dilution of ferromagnetic nanoparticles, the magnitude of the applied magnetic field, maximally strained droplet shape.

### 3.4.11 Statistics.

In experiments involving zebrafish embryos, the sample size was chosen so that new data points would not significantly change the standard deviation. No samples were excluded from the analysis and the analysis of all the data was done by automated software to ensure full blinding and avoid biases in the analysis. No randomization of the data was used.

## 3.5 Author contributions

The work described in this chapter was the result of a collaboration with others (see Permissions and Attributions). The particular contributions by the author of this dissertation include the development of the code and the running of the analysis required to transform experimental images of droplets in embryonic zebrafish tissue into measurements of mechanical stress, as well as associated length scale and temporal autocorrelation analysis.

## 3.6 Permissions and Attributions

1. The content of chapter 3 is the result of a collaboration with Alessandro Mongera, Payam Rowghanian, Hannah Gustafson, DA Kealhofer, Emmet Carn, Friedhelm Serwane, Adam Lucio, James Giammona, and Otger Campàs., and has previously appeared in the journal Nature [2]. Parts of that work are reproduced here in accor-

---

[2] A Mongera, P Rowghanian, HJ Gustafson, **E Shelton**, DA Kealhofer, EK Carn, F Serwane, AA Lucio, J Giammona, O Campàs. A fluid-to-solid jamming transition underlies vertebrate body axis elongation *Nature* 561, 401-405 (2018)

dance with rights retained by authors. To find the work as it originally appeared: `https://doi.org/10.1038/s41586-018-0479-2`.

# Chapter 4

# Mechanics of Vertebrate Somite Formation

## 4.1 Introduction

During embryonic development, signaling events coordinate cell behaviors to form functional structures, including organs and embryonic precursors of adult structures [1, 86]. The molecular players and mechanisms involved in orchestrating morphogenesis, both in early embryos and during organ formation, have been studied extensively [1]. However, sculpting embryonic structures also involves spatiotemporal variations in tissue mechanics that progressively bring the tissue into shape [87, 88, 89]. In this sense, embryonic tissues are active materials with the remarkable ability to self-shape, but it remains unclear how this is achieved in specific cases.

The segmentation of the vertebrate body along its anteroposterior (AP) axis into periodic, bilaterally symmetric pairs of somites, or somitogenesis (Supplementary Movie 1), is a key process in vertebrate development that lays the foundation for all skeletal muscles and vertebrae in adults [90, 6, 91, 92]. Several signaling pathways are involved in coordinating cell behaviors in space and time during the segmentation process [90, 93, 94]. Synchronization of genetic oscillators in neighboring cells of the PSM sustain traveling waves in the tissue that emerge at the posterior end of the body [95, 96, 91, 97], travel anteriorly and eventually arrest, defining the location of the new somite along the AP axis [98, 93, 91, 96]. Eph-ephrin interactions between cells at the prospective somite boundary regulate Rho and Rac activity [99, 100, 101, 102], boundary cell de-adhesion and ECM deposition [103, 104, 105], defining the initial molecular signatures of mechanical changes during somitogenesis. However, the tissue-scale mechanical transformations that emerge from all these molecular events and shape the somites are unknown.

Mechanics has long been recognized to play a role in somite morphogenesis [106, 107, 108, 109]. Previous observations of rounding and spontaneous segmentation of mesodermal explants in chick and quail [110], as well as the rounding of explanted somite tissue in zebrafish [111], suggested that tissue surface tension alone may drive segmentation, akin to a Plateau-Rayleigh instability in fluids [112]. However, recent experiments have shown that the PSM tissue is in a solid-like state at the timescales of somite formation [77], indicating that a different physical mechanism may be at play to shape somites. Here, we provide direct *in vivo* and *in situ* measurements of tissue mechanics during somite formation, spatiotemporal analysis of actomyosin dynamics, as well as computer simulations, to reveal the physical mechanism of somite formation in zebrafish development.

## 4.2 Results

### 4.2.1 Nascent somite boundaries shorten and straighten as somites mature.

Since the defining morphological event initiating the formation of a new somite in the PSM is the appearance of its posterior boundary [92], we imaged its formation and monitored it over time by backtracking the forming somite boundary from its well-formed mature state (Fig. 4.1a,b; Methods; Supplementary Movie 2). The nascent posterior somite boundary appears initially contorted and sharpens over time. While the straight end-to-end distance of the nascent boundary, $L_s$, varies only slightly during somite formation (fixed largely by the mediolateral extent of the PSM), the boundary contour length $L_c$ decreases by over 50% (Fig. 4.1b,c). This leads to the progressive straightening of the boundary (Fig. 4.1d), characterized by the ratio $L_s/L_c$, over approximately 1 hour and ends with a nearly perfectly straight somite boundary ($L_c/L_s \simeq 0.98$). In order to temporally align (and stage) somite formation in different embryos and perform statistical analysis, we took advantage of the fact that boundary straightening during the formation of a new somite (Fig. 4.1b,d) displays a sigmoid behavior (Fig. 4.1d). We define a temporal benchmark ($t = 0$ minutes) at the center point of this sigmoid (Methods). By this convention, $t$ corresponds to the time elapsed since the somite's posterior boundary has reached B-1 or, equivalently, since the somite itself has reached S0. The observed progressive straightening of the prospective somite boundary suggests that mechanical stresses may be changing along the boundary during somite formation.

### 4.2.2 F-actin and myosin II accumulate at the forming somite boundary, albeit non-synchronously.

Previous studies in *Drosophila* have shown that actin and myosin II accumulation at compartment boundaries are important for their formation and maintenance [113, 102, 114, 115, 116]. In zebrafish, enrichment of F-actin at mature somite boundaries has been previously observed [117, 118], suggesting that temporal changes in actomyosin activity may play a role in somite formation. To quantify their spatiotemporal dynamics at the forming boundary and relate them to the observed boundary straightening, we monitored actin and myosin II during boundary formation (Fig. 4.1e; Methods). Kymographs showing the spatiotemporal changes in F-actin and myosin II at the forming boundary indicate that both increase as the boundary shortens and straightens (Fig. 4.1f,g), with an average increase of approximately 180% and 150% in signal from S-2 to S2, respectively (Fig. 4.1h). While the increase in F-actin and boundary straightening occur simultaneously, accumulation of myosin II is delayed by approximately 15 min (Fig. 4.1d,h). Despite this delay, both F-actin and myosin II accumulate at the forming somite boundary as it straightens, suggesting that mechanical tension increases at the forming boundary during somite formation.

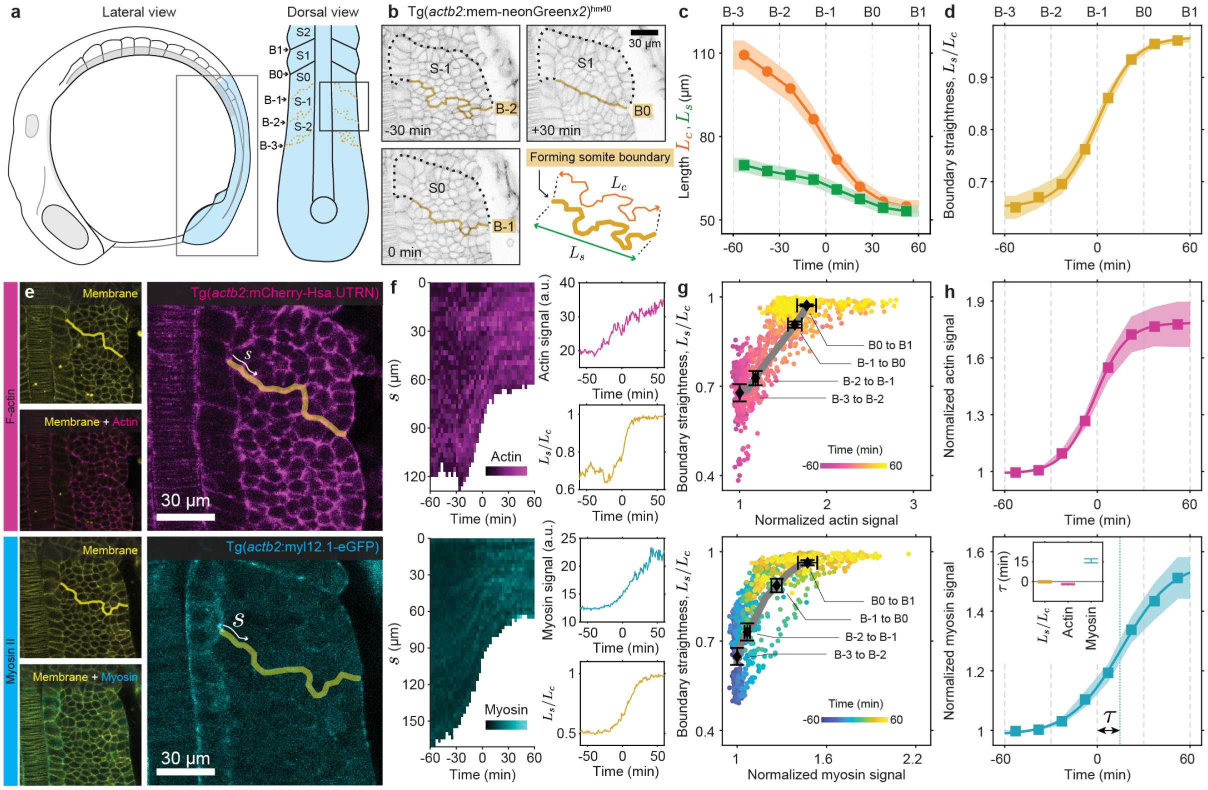

Figure 4.1: **Evolution of boundary morphology and F-actin and myosin II distributions at the forming boundary.** **a**, Sketches showing a lateral view of a 12-somite stage zebrafish embryo and a dorsal view of posterior tissues showing somites at different maturation stages (from S-2 to S2). **b**, Confocal sections of a forming somite in Tg(*actb2*:mem-neonGreen-neonGreen)$^{\mathrm{hm40}}$embryos at S-1, S0 and S1, with its boundaries highlighted with dashed lines (posterior nascent boundary, yellow; other boundaries, black). A sketch of the forming posterior boundary is shown with the contour and end-to-end lengths, $L_c$ and $L_s$, respectively, defined. **c-d**, Temporal evolution of $L_c$ (orange; **c**), $L_s$ (green; **c**) and the boundary straightness $L_s/L_c$ (**d**), with sigmoid fits shown as continuous lines; average: $n = 110$ (22 somites; 5 timepoints) from 11 embryos. **e**, Confocal sections of the segmenting anterior PSM showing both membrane and F-actin (top) and membrane and myosin II (bottom) signals. Boundary masks are shown in yellow, and $s$ is the contour distance along the boundary. **f**, Kymographs showing the temporal increase in F-actin (top) and myosin II (bottom) along boundary. Examples of the temporal evolution of the average F-actin (top) and myosin II (bottom) signals at the boundary are shown together with the time evolution of the boundary straightness. Average: $n = 120, 100$ (top, bottom) (12, 10 somites; 10 timepoints) from 6, 5 embryos, respectively **g**, Relation between boundary straightness and F-actin (top) or myosin II (bottom) during somite formation. **h**, Temporal evolution of F-actin (top) and myosin II (bottom) average densities at the forming boundary. Average: $n = 60, 50$ (top, bottom) (12, 10 somites; 5 timepoints) from 6, 5 embryos, respectively (**g-h**). Solid line shows sigmoid fit to average. Inset shows the temporal shift $\tau$ for F-actin ($-1.9 \pm 0.5$ min) and myosin II ($15.8 \pm 0.5$ min). Error bands = SE.

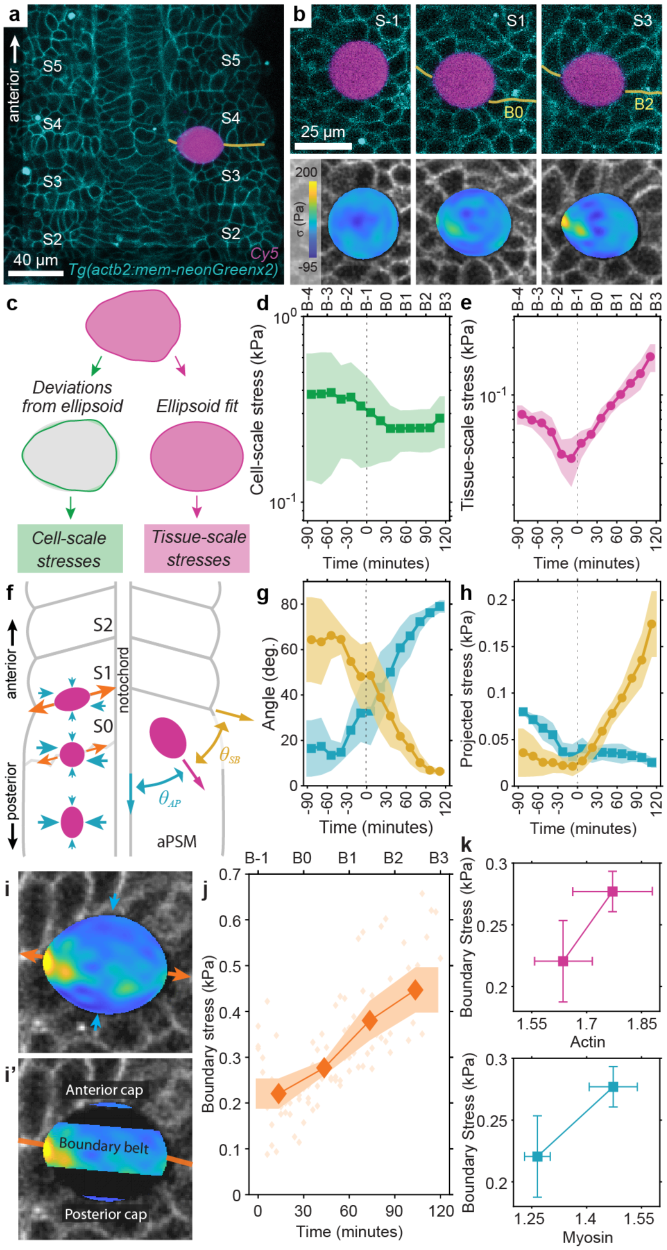

Figure 4.2: **Mechanical stresses during somitogenesis.** **a**, Confocal section of a droplet (magenta) at the boundary between somites S3 and S4 (membrane label, cyan; somite boundary B3 shown in yellow). **b**, Confocal sections of the temporal evolution (S-1 to S3) of a droplet at the somite boundary (top) and corresponding droplet stress maps (bottom). **c**, Sketch of the decoupling of cell and tissue scale stresses (Methods). **d-e**, Time evolution of cell-scale (**d**) and tissue-scale (**e**) stresses. Average: $n = 20$ (4 droplets; 5 timepoints). **f**, Sketch showing the evolution of stresses during somitogenesis: increasing somite boundary stresses progressively compete with ML stresses in the PSM. Definition of the angles between droplet ellipsoidal elongation

Figure 4.2: and the AP (blue) and somite boundary (yellow) directions, $\theta_{\text{AP}}$ and $\theta_{\text{SB}}$ respectively. **g-h**, Time evolution of the direction of droplet elongation (**g**), quantified by $\theta_{\text{AP}}$ (blue) and $\theta_{\text{SB}}$ (yellow), and of the projected magnitude of stresses (**h**) along the AP and somite boundary directions. Average: $n = 20$ (4 droplets; 5 timepoints) **i-i'**, Confocal section of a droplet (stress colormap as in **b**) at a somite boundary (membrane label) with arrows indicating relative stresses on drop (**i**), and definitions of boundary belt and anterior and posterior caps (**i'**). Orange line indicates somite boundary (bottom). **j**, Temporal evolution of boundary stress. Average: $n = 15$ (3 droplet; 5 timepoints) **k-l**, Boundary stress, average: $n = 30$ (3 droplets; 10 timepoints), as a function of F-actin (**k**) and myosin II (**l**) at the somite boundary, average: $n = 120, 100$ (12, 10 somites; 10, 10 timepoints), respectively. Error bands = SE.

### 4.2.3 Mechanical stresses reorient in the tissue during somite formation.

To directly quantify the temporal evolution of mechanical stresses in the tissue during somite formation, we employed magnetically-responsive oil droplets [77, 81]. After injecting a fluorescently-labeled droplet in the PSM of zebrafish embryos at the 4-6 somites stage, we monitored it over time as somites formed (Fig. 4.2a,b; Methods; Supplementary Movies 3 and 4). To do so, we captured a 3D timelapse of each droplet, quantified its deformations using automated 3D reconstruction and analysis software [119, 85] (Fig. 4.2c; Methods), and obtained both cell-scale and supracellular (tissue-scale) stresses after calibrating the droplet *in situ* and *in vivo* (Fig. 4.2c; Methods).

The average cell-scale stresses, namely those stresses occurring at cellular length scales [119] (Methods), show no significant temporal change throughout somite formation, maintaining a value of approximately 200 Pa (Fig. 4.2d). These measurements are in agreement with previously measured values of cell-scale stresses in the PSM, which were shown to be spatially uniform in the tissue [77]. In contrast, tissue-scale stresses, obtained from the ellipsoidal mode of droplet deformation [119], displayed changes in both magnitude (Fig. 4.2e) and orientation (Fig. 4.2f,g) as the somites formed, revealing changes in mechanical stress anisotropy in the tissue. Before somite formation began ($t = -60$ minutes; B-3), droplets were initially oriented along the AP axis in the PSM due to the presence of mediolateral (ML) stress anisotropy, as previously reported [77]. As somite formation proceeded, tissue-scale anisotropic stresses substantially decreased (from $62 \pm 15$ Pa at B-3 to $35 \pm 11$ Pa at B-1) and reached a minimum just before B-1 ($t = 0$ minutes), with the direction of stress anisotropy changing in the process (Fig. 4.2e,g). After B-1, the magnitude of stress anisotropy strongly increased, reaching values ($134 \pm 48$ Pa) 200% larger than those in the PSM, and the droplet aligned with the direction of the future somite boundary (Fig. 4.2g). These stress measurements show that tension along the nascent somite boundary progressively increases and competes with the ML stresses existing in the PSM (Fig. 4.2f), with the stress component oriented along the future somite boundary overcoming ML stresses at B-1 and increasing thereafter (Fig. 4.2h).

### 4.2.4 Mechanical stresses at the somite boundary strongly increase during somite formation.

Since tissue-scale stresses reorient in the direction of the somite boundary and increase over time, stresses generated at the forming somite boundary may be responsible for driving somite formation. In order to measure the stress anisotropy at the somite boundary, we selected droplets located in the middle of the forming boundary (from the moment when a boundary is visible at B-1), and analyzed the stress anisotropy between the direction defined by the somite boundary and the perpendicular one (Fig. 4.2i; Methods). The magnitude of boundary stress anisotropy is larger than tissue-scale stresses, indicating that maximal stresses in the tissue occur at the forming somite boundary (Fig. 4.2j). Moreover, boundary stresses increase over time, with their value doubling from just after B-1 (220 ± 33 Pa) to B3 (447 ± 49 Pa). The observed increase in boundary stress correlates with the progressive accumulation of actomyosin at the forming boundary (Fig. 4.2k), indicating that the measured spatial localization and temporal increase of boundary stresses are driven by the progressive actomyosin accumulation at the forming somite boundary.

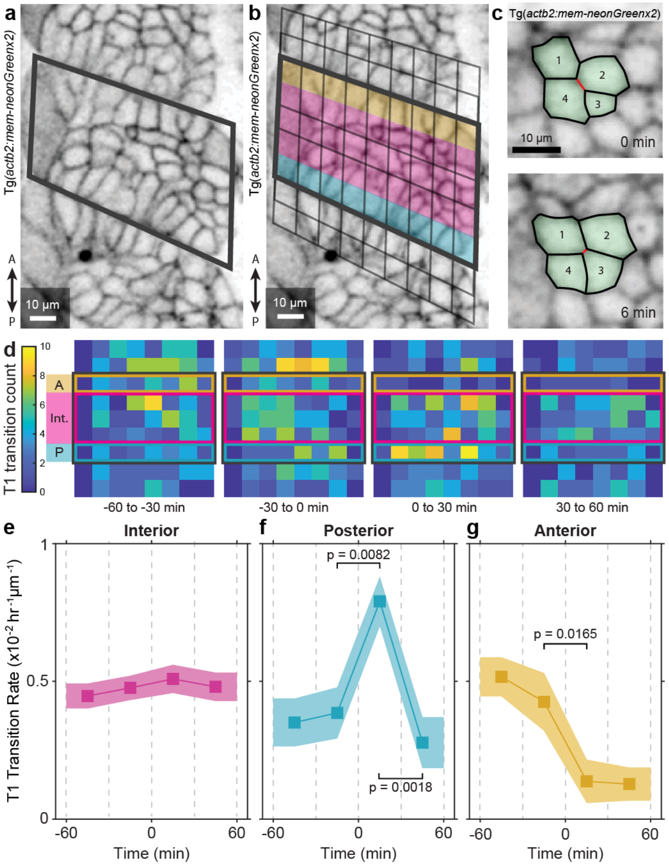

Figure 4.3: **Spatiotemporal changes in T1 transition rates during somite formation.** **a-b**, Confocal section of a somite (membrane label) with its boundary approximated as a quadrilateral (gray; **a**), and with a grid overlay (light gray; **b**) defining the different regions within the somite (yellow = anterior boundary, magenta = somite interior, cyan = posterior boundary) and neighboring tissue. **c**, Example of a T1 transition event shown with annotated confocal sections (membrane label). **d**, Time evolution of the T1 transitions' spatial distribution. **e-g**, Time evolution of average T1 transition rates for interior (**e**), posterior (**f**), and anterior (**g**) regions. Average: $n = 42$ (14 somites, 3 time intervals) from 7 embryos. Error bands = SE.

### 4.2.5 Cell rearrangements show the regional fluidization of the tissue adjacent to the forming somite boundary.

The measured values of boundary stress are larger than the previously measured residual (yield) stress in the PSM [77], suggesting that boundary stresses may fluidize adjacent tissue areas. Since plastic remodeling (or fluidization) of the tissue requires cell rearrangements (T1 transitions), we quantified the spatiotemporal dynamics of T1 transition rates during somite formation. To do so, we defined a quadrilateral grid on each somite (Fig. 4.3a,b; Methods), recorded the location and time of each neighbor exchange event (T1 transition; Fig. 3c), and analyzed the spatial distribution of neighbor exchanges within four 30 min periods from t=-60 min to t=60 min (B-3 to B1; Fig. 4.3d; Methods). The interior of the somite (excluding the regions directly adjacent to somite-somite boundaries; Fig. 4.3b,d) displayed uniform T1 transitions throughout somitogenesis, with a constant average rate equal to its value in the PSM before somite formation (from S-2 to S-1) (Fig. 4.3e; Methods). In contrast, T1 transition rates at the boundaries displayed significant changes during somite formation. The rate of T1 transitions in the tissue adjacent to the forming posterior somite boundary showed a sharp ($>$ 2-fold) increase between t=0 (B-1) and t=30 min (B0), exactly the period when stresses along the somite boundary become dominant and boundary straightening occurs (Fig. 4.3f). This localized increase in T1 transitions reveals a regional fluidization of the tissue adjacent to the forming posterior somite boundary, caused by the large boundary stresses driving its shortening and straightening. Unlike the posterior region, the tissue adjacent to the anterior somite boundary displayed a significant drop in T1 transition rate after t=0 (Fig. 4.3g). Here, the T1 rate became more than 3-fold lower than the average value in the somite interior and the PSM, indicating that the anterior region is rigidifying further than the PSM, possibly due to cell attachment at the more mature boundary. This reveals spatiotemporal changes in the somite physical state over the course of somitogenesis, with the fluidization of the tissue adjacent to the posterior boundary occurring as the tissue surrounding the anterior boundary rigidifies. Together with previous measurements of stress relaxation in the paraxial mesoderm [120, 77], our results indicate that at the timescales of somite formation (30 minutes) both the interior of the somite and its anterior boundary are in a solid state (albeit with a more rigid anterior boundary), while the posterior boundary is transiently fluidized during the physical segmentation of the PSM.

### 4.2.6 Active tension fluctuations at cell-cell contacts and an increase in somite boundary tension are necessary to reproduce somite morphogenesis.

Our observations of increasing myosin II and actin levels at the nascent somite boundary, concomitant with boundary straightening and increasing boundary stresses, strongly suggest that an increase in tension at the somite boundary mechanically drives segmentation events. To test this hypothesis, we performed simulations of the mechanics of somitogenesis using an active foam description [120] (Methods). Starting from a population of cells in a rectangular geometry (Fig. 4.4a), we defined different cell-cell contacts depending on whether they are located at the lateral boundary, at a somite boundary (heterotypic contacts) or in neither of those (homotypic contacts). To computationally account for our observations that cell-scale stresses do not change in time and that boundary stresses increase, we set the average value of homotypic tensions to a constant $T_0$, and made the average tensions at heterotypic cell-cell contacts, $T_H$, undergo sequential ramp ups (from $T_0$ at B-3 to a maximal value $T_M$ at B1) following the observed increase in actomyosin at the somite boundary (Fig. 4.4b,c; Methods), including the observed delay in myosin II increase (Fig. 4.1h). Beyond their average value, cell-cell contact tensions fluctuate and drive cell-cell contact length fluctuations (Fig. 4.4d), as previously reported [77]. Consequently, we simulated tension fluctuations of constant amplitude $\Delta T$ and characteristic persistence time of 90 s, as observed experimentally [77]. Finally, we set the value of the tension at the lateral boundary to a constant $T_L$ because measurements of F-actin and myosin II at the lateral boundary show no changes over time (Fig. 4.4e).

Values of the maximal heterotypic tension, $T_M$, larger than twice the value of the lateral boundary tension, $T_L$, namely $T_M > 2T_L$, led to complete somite separation (Fig. 4.4f). Below this threshold ($T_M < 2T_L$), adjacent somites shared a boundary of finite length (Fig. 4.4f; Supplementary Movie 5), with its straightness depending on how much heterotypic tensions increase at the somite boundary ($T_M/T_0$), irrespective of the value of the tension $T_L$ at the lateral boundary (Fig. 4.4g,h). Increasing heterotypic tension up to 3 times homotypic tensions ($T_M/T_0 = 3$) efficiently straightened the somite boundary, but not much more above this value (Fig. 4.4h).

Beyond the increase of tension at the forming somite boundary, boundary straightness depended also on the magnitude of active tension fluctuations, $\Delta T/T_0$. The somite boundary could not straighten to experimentally observed values without tension fluctuations (Fig. 4.4i), as in this case the only cell rearrangements present were those induced by the tension increase at the somite boundary, with no cell rearrangements facilitated by active tension fluctuations [120]. Increasing the magnitude of tension fluctuations up to approximately $\Delta T/T_0 \simeq 0.6$ led to more straight somite boundaries (Fig. 4.4j). Beyond this point, increasing tension fluctuations did not help straighten the somite boundary significantly more. Moreover, the statistical variation in boundary straightness was maximal for vanishing tension fluctuations (Fig. 4.4j), indicating large deviations from the straight boundary, and decreased with increasing fluctuations up to about $\Delta T/T_0 = 0.6$, defining a sharper somite boundary with minimal variation for this value. In contrast, deformities in somite shape (somite angle; Fig. 4.4k) and deviations from the midline (positional deviations; Fig. 4.4k) showed a minimum at $\Delta T/T_0 \simeq 0.7$. These results indicate the existence of an optimal value of tension fluctuations ($\Delta T/T_0 \simeq 0.6 - 0.7$) leading to maximally robust somite formation.

Fitting the experimentally observed temporal increase in boundary straightness and its maximal observed value, we found best agreement between simulations and observations for $T_M/T_0 \simeq 3$ and $\Delta T/T_0 \simeq 0.6$. To estimate the value of the cell tension at the lateral boundary, $T_L$, we measured the angles $\theta_H$ and $\theta_L$ formed by two cells forming heterotypic and homotypic contact, respectively, at the lateral boundary (Fig. 4.4l). While the angle $\theta_L$ remains constant and close to 180 (flat lateral boundary) away from the somite boundary, the angle $\theta_H$ at the forming somite boundary decreases significantly throughout somitogenesis (Fig. 4.4m), in line with our measurements of actomyosin accumulation at the forming boundary and increase in boundary stress. The value of $\theta_H$ at B1 allowed us to determine the value of $T_L/T_0$, locating wild type zebrafish somitogenesis in the parameter space (Fig. 4.4f). These results indicate that cells at the somite boundary increase the boundary tension during somite formation to the minimal value necessary to fully straighten the boundary, and that cells in the tissue generate an optimal level of active tension fluctuations to ensure robust somite morphogenesis.

## 4.3 Discussion

Altogether, our experimental and computational results show that somites are physically set apart from the PSM by an actomyosin-driven increase in anisotropic stress at the forming somite boundary that fluidizes the immediately adjacent tissue, thereby enabling tissue remodeling and the shaping of the somite. Moreover, we find that zebrafish somitogenesis occurs with close to optimal cell-cell contact tension fluctuations, which help robustly define straight somite boundaries with minimal morphological somite defects.

In contrast to observations using tissue explants suggesting that somites may form from a mere increase in tissue tension all around the fluid-like somite tissue, our results indicate that somites are physically segmented from the solid-like PSM following a highly localized increase in actomyosin-generated tension at the forming somite-somite boundary (between B-1 and B0), with no change in actomyosin-generated tension at the lateral boundary. In addition, we find that the somite interior remains in a solid-like state (as the PSM) during somite formation, with fluidization occurring only in the tissue immediately adjacent to the straightening posterior boundary. Rather than the rounding of fluid-like tissue, somites seem to physically form by a sharp increase in tension at the forming somite boundary that drives a transient and localized tissue fluidization to facilitate tissue remodeling as the somite is sculpted. While our simulations of the physical process of somite formation reproduce both elongated somites that maintain contact, as observed in zebrafish, as well as round separated somites, resembling those recently observed in trunk organoids [121], it remains to be seen if this physical mechanism of somitogenesis is shared across vertebrate species. It is possible that similar physical events occur in distinct species, albeit with different cell behaviors and molecular control, as suggested by the observed differences in somite actin distribution in amniotes [100].

The observed actomyosin accumulation at the somite boundary is reminiscent of boundary formation in other systems [113, 102, 115, 114], where actomyosin accumulation at the boundary has been shown to maintain separate physical compartments of the tissue. However, in vertebrates, mature somite boundaries are characterized by the presence of extracellular matrix [106, 105, 122, 103], indicating that the increase in boundary stresses reported here may be necessary to physically segment somites, but not for boundary maintenance. Understanding the role of actomyosin-driven boundary stress in the maintenance of somite boundaries will require further investigation.

The notion that mechanics can help achieve robust somitogenesis was recently put forward in the context of lateral symmetry between somites [111]. Albeit in a different context, our results support the idea that mechanics enables robust somite formation, as the amplitude of tension fluctuations appears to be optimally tuned to enable maximal somite boundary straightening with minimal variation in boundary straightness and minimal somite morphological defects. This result indicates that tension fluctuations may play an important role in embryonic development, not only in the control of fluid-to-solid transitions [120, 77], but also facilitating the robust sculpting of embryonic structures.

Our findings highlight the need to connect genetic and molecular aspects of somitogenesis with cell and tissue mechanics to obtain a holistic view of somite formation and, more generally, of how functional embryonic structures are sculpted during embryonic development.

## 4.4 Acknowledgements

We thank all members of the Campàs group for their comments and help, and B. Shelby, G. Stooke-Vaughan, S.-T. Yen and the UCSB Animal Research Facility for help with zebrafish care. We also thank Sean Megason (Harvard University) for kindly providing the Tg(actb2:memCherry2)$^{hm29}$ transgenic line, and C.-P. Heisenberg (IST, Austria) for kindly providing the Tg(*actb2*:myl12.1-eGFP) and Tg(*actb2*:mCherry-Hsa.UTRN) transgenic lines. The Tg(actb2:mem-neonGreen-neonGreen)$^{hm40}$ line was generously provided before publication by Toru Kawanishi and Ian Swinburne in Sean Megason's lab (Harvard University). This work was supported by the National Institute of General Medical Sciences (R01GM135380 to EMS and OC) and the Eunice Kennedy Shriver National Institute of Child Health and Human Development of the National Institutes of Health (R01HD095797 to OC). We acknowledge support from the Center for Scientific Computing from the CNSI, MRL: an NSF MRSEC (DMR-1720256) and NSF CNS-1725797. The project was partially supported by the Deutsche Forschungsgemeinschaft (DFG, German Research Foundation) under Germany's Excellence Strategy – EXC 2068 – 390729961– Cluster of Excellence Physics of Life of TU Dresden.

## 4.5 Author Contributions

The work described in this chapter was the result of a collaboration with others (see Permissions and Attributions). The particular contributions by the author of this dissertation include designing the research (in collaboration with Otger Campas), performing all experiments, and analyzing the data. Ben Grossman, Ray Wu, and Marie Pochitaloff also assisted in the analysis of data.

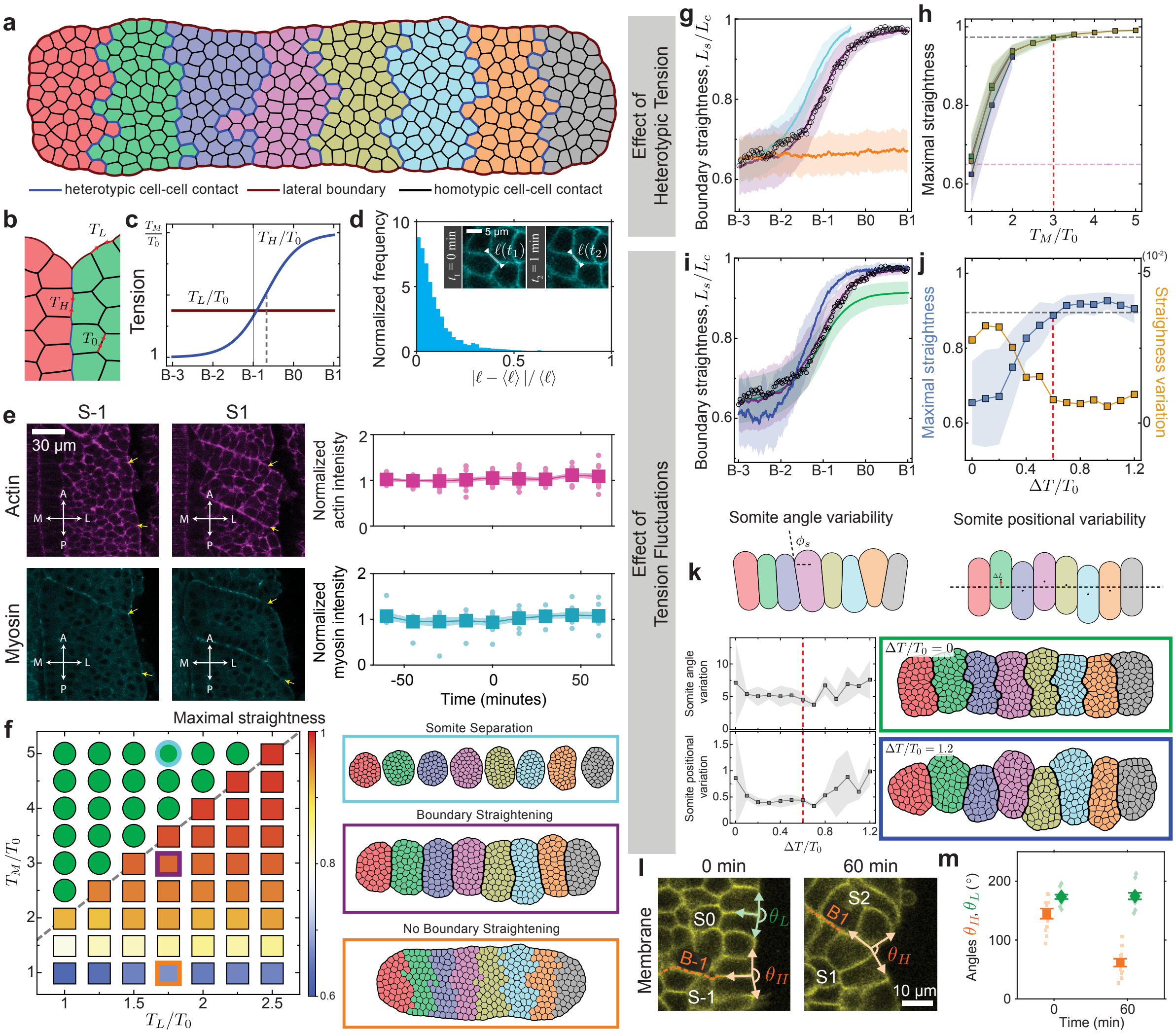

Figure 4.4: **Simulations of somite formation.** **a**, Initial state of somite formation simulation with prospective somites uniquely colored. Heterotypic (blue) and homotypic (black) cell-cell contacts, as well as the lateral boundary (maroon), are indicated.

Figure 4.4: **b**, Schematic diagram showing tensions at lateral boundaries ($T_L$), heterotypic contacts ($T_H$), and homotypic contacts ($T_0$). **c**, Imposed time evolution of the normalized heterotypic and lateral tensions, $T_H/T_0$ and $T_L/T_0$, respectively, with $T_H$ saturating to a maximal value $T_M$. **d**, Normalized frequency of the magnitude of cell-cell contact length fluctuations in the anterior PSM (reanalyzed from [77]). Inset shows junction length changes in 1 min interval. **e**, Confocal sections showing the F-actin (top) and myosin II (bottom) density during somite formation (left) and the time evolution of their average density at the lateral boundary (right). Individual somite measurements in light circles, averages in dark squares; $n = 6, 6$ somites (actin, myosin; $-60 < t < -45$ min); $n = 12, 8$ somites (actin, myosin; $t > -45$ min); error band = SE. **f**, Somitogenesis phase diagram, showing how somite formation depends on $T_L/T_0$ and $T_M/T_0$ ($\Delta T/T_0 = 0.6$). For $T_M/T_L > 2$ somites completely separate (cyan circle; cyan rectangle showing configuration, right). For $T_M/T_L < 2$, somites do not completely separate and share a boundary with a maximal straightness (color coded value at B1) that depends mostly on $T_M$ (for fixed $\Delta T/T_0$). Configurations for parameter values estimated from experiments ($T_L/T_0 = 1.75$, $T_M/T_0 = 3$, $\Delta T/T_0 = 0.6$; purple, middle) and limiting case with no boundary tension increase ($T_M/T_0 = 1$; orange, bottom) are shown. **g-i**, Experimental (black circles) and simulated (lines) time evolution of boundary straightness $L_s/L_c$. Simulations for different values of $T_M/T_0$ (**g**; same color code as in **f**; $\Delta T/T_0 = 0.6$). Maximal boundary straightness (**h**; boundary straightness at B1, $L_s/L_c\,(B1)$) as a function of $T_M/T_0$ for different $T_L/T_0$ values ($\Delta T/T_0 = 0.6$), showing no significant effects of the lateral tension on boundary straightening. Simulations for different magnitudes of tension fluctuation $\Delta T/T_0$ (**i**; $\Delta T/T_0 = 0$ (green) ,$\Delta T/T_0 = 0.6$ (purple), $\Delta T/T_0 = 1.2$ (blue); $T_M/T_0 = 3$ and $T_L/T_0 = 1.75$). **j**, Dependence of the maximal boundary straightness (blue; $L_s/L_c\,(B1)$) and the standard deviation of maximal boundary straightness (yellow; $\sigma_{L_s/L_c(B1)}$) on $\Delta T/T_0$ ($T_M/T_0 = 3$ and $T_L/T_0 = 1.75$). **k**, Variability of final somite angle (top left) and position (top right) as a function of $\Delta T/T_0$ (bottom left). Final configurations of simulated somite formation for vanishing fluctuations ($\Delta T/T_0 = 0$; green) and large fluctuations ($\Delta T/T_0 = 1.2$; blue). Error band = SD in **g-k**. **l**, Confocal section showing the angle formed between adjacent cells from the same somite at the lateral boundary ($\theta_L$) and cell on different somites ($\theta_H$; at the somite boundary). **m**, Measured values of $\theta_L$ and $\theta_H$ at S0 and S2. Average: $n = 12$ somites (6 embryos); error bar = SE.

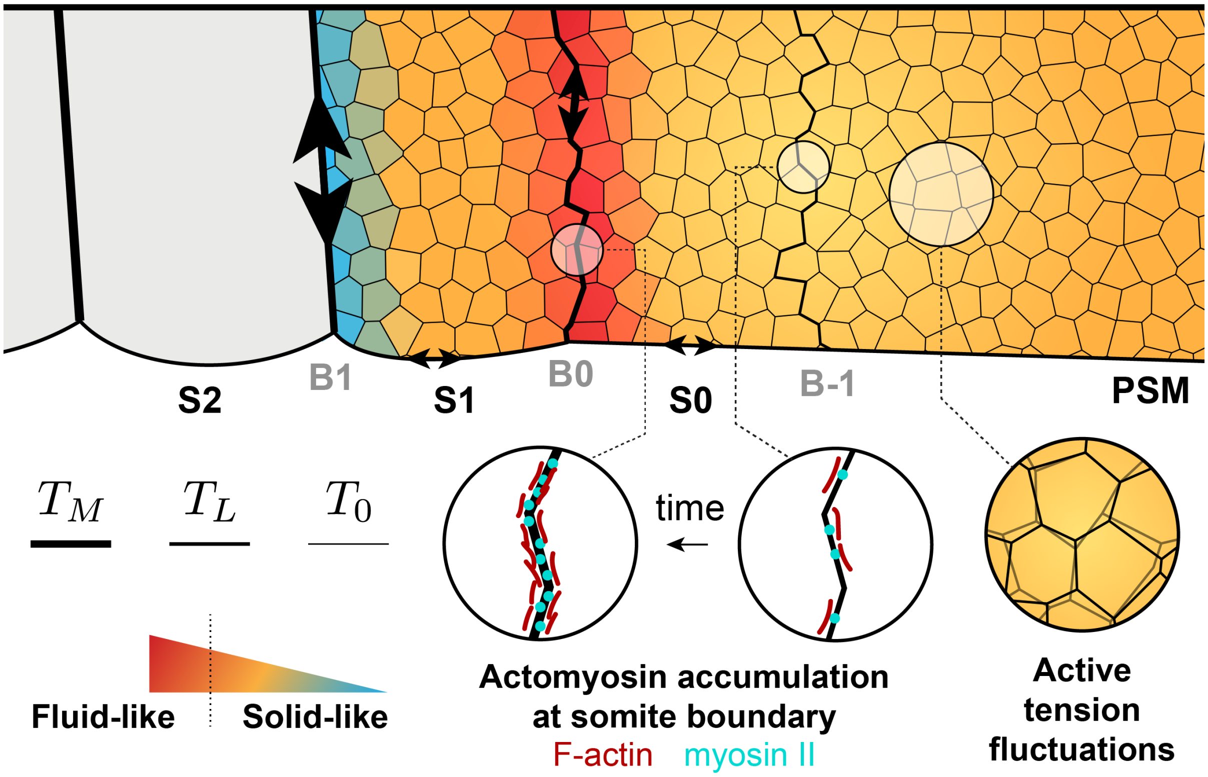
S2
B1
S1
B0
S0
B-1
PSM
$T_M$
$T_L$
$T_0$
time
Fluid-like
Solid-like
Actomyosin accumulation at somite boundary
F-actin
myosin II
Active tension fluctuations

Figure 4.5: **Physical mechanism of somite formation.** Sketch detailing the main events involved in mechanically forming a somite. A progressive accumulation of F-actin and myosin II at the nascent posterior boundary of the forming somite (S0) causes an increase in boundary tension that fluidizes the tissue adjacent to the forming posterior boundary (B-1 to B0), enabling tissue remodeling. Once mature (B0), the tissue adjacent to the boundary rigidifies again. Optimal actomyosin-generated tension fluctuations facilitate the process, enabling robust somite boundary formation. Somites are physically sectioned off the PSM by the boundary tension increase and fluidization at the posterior boundary.

## 4.6 Methods

### 4.6.1 Zebrafish husbandry and transgenic lines.

Zebrafish (*Danio rerio*) were maintained as previously described [78]. Animals were raised and experiments were performed following all ethical regulations and according to protocols approved by the Institutional Animal Care and Use Committee (IACUC) at the University of California, Santa Barbara. Transgenic lines Tg(*actb2*:mem-neonGreen-neonGreen)$^{hm40}$ or Tg(*actb2*:memCherry2)$^{hm29}$ [123] were used to visualize cell membranes, and Tg(*actb2*:mCherry-Hsa.UTRN) [124] and Tg(*actb2*:myl12.1-eGFP) [125] were used to visualize F-actin and myosin II, respectively.

### 4.6.2 Imaging.

Embryos were mounted in 1% low melting point agarose (E3 media containing 0.01% Tricaine) at approximately the 10 somites stage and imaged at 25°C using a laser scanning confocal microscope (LSM 710 Carl Zeiss Inc.). Images were acquired at 15 second intervals for *in situ* droplet actuation experiments and at 1 to 3 minute intervals for time lapse imaging of somite formation, depending on the experiment. All imaging of embryos was done using a 40× water immersion objective (LD C-Apochromate 1.1 W, Carl Zeiss). Imaging of F-actin and myosin II was done with spatial resolution ranging from 0.35-0.69 µm. Volumetric images of droplets was done at 0.35 µm spatial resolution, and 4.0 µm z-steps.

After timelapse imaging, embryos were removed from agarose and imaged laterally to determine the position of the droplet along the AP axis. All stress measurements were performed between the 14 and 16 somites stages.

### 4.6.3 Quantification of somite boundary morphology.

Forming somite boundaries were identified and annotated manually using sequences of confocal sections of Tg(*actb2*:mem-neonGreen-neonGreen)$^{\mathrm{hm40}}$ or Tg(*actb2*:memCherry2)$^{\mathrm{hm29}}$ embryos. First, we identified the location of the mature somite boundary in the final frame of the timelapse sequence. Next, we identified the boundary in the previous frame in the sequence, using the most recently analyzed frame as a reference. At each frame, boundary annotations were recorded as ordered sets of coordinates. The boundary contour length $L_c$ was computed by summing the length of line segments connecting the coordinates along the contour. The straight end-to-end distance of the somite boundary, $L_s$, was computed as the distance between the first and last coordinates of the contour. Somite-somite boundaries were annotated at 1 minute or 3 minute increments depending on the experiment, whereas lateral boundaries were traced at 15 minute intervals. Adaxial cell boundaries were not included in boundary annotations.

### 4.6.4 Temporal registration of different embryos and staging of somite formation.

Data sets collected from different embryos were temporally aligned with each other using the temporal evolution of the straightness measure, namely $m_s(t) \equiv L_s/L_c$. For each somite boundary in each experiment, the measured straightness was fit to the function $m_s(t) = A/(1 + e^{(t-B)\times C}) + D$, where $A$ specifies the amplitude, $B$ specifies time of half-time between initial and final states, $C$ specifies the ramping rate, and $D$ specifies the baseline offset. For each embryo, we associated the half-time $B$ with the time of stage B-1 of somite boundary formation (Fig. 4.1b), as the straightening corresponds to the nascent posterior boundary of somite S0 [126]. Experiments in different embryos were then temporally aligned by registering their half-times and shifting them all to t=0. Therefore, t=0 corresponds to the stage B-1 of somite boundary formation. The stages S(N) of somite formation (S0 referring to the currently forming somite, S1 referring to the most recently formed somite, and so on) and their posterior (caudal) and anterior boundaries, namely B(N-1) and B(N) respectively, were denoted following established nomenclature [126] (Fig. 4.1b). Boundaries at stages B(N-1) (N = -2, -1, 1, 2, ...) occured at times $t = N\,T$ relative to stage B-1 ($t = 0$ min), with $T = 30.0 \pm 2.7$ min being the period of somite formation in our experiments (wild type zebrafish embryos at 25°C [76]).

### 4.6.5 Quantification of F-actin and myosin II fluorescence signal at somite-somite and lateral boundaries.

Quantification of the F-actin signal at the somite boundary was obtained using an outcross of Tg(*actb2*:mCherry-Hsa.UTRN) and Tg(*actb2*:mem-neonGreen-neonGreen)$^{\mathrm{hm40}}$ to visualize F-actin and membranes simultaneously, whereas quantification of myosin II signal at the somite boundary was done using an outcross of Tg(*actb2*:myl12.1-eGFP) and Tg(*actb2*:memCherry2)$^{\mathrm{hm29}}$ to visualize myosin II and membranes simultaneously. Intensities of actin and myosin II along the boundary contour were computed from boundary coordinates (see above) and fluorescent images sequences using custom Matlab scripts. Traced boundary coordinates were converted into a Polyline ROI object, which was then converted into a binary array using the function createMask(). This binary array was then dilated with a disk shaped structuring element using the function imdilate(), resulting in boundary masks approximately 3 µm in width. These masks were used at each frame to compute the average signal intensity along the boundary at each timeframe. We determined if considerable photobleaching occurred in a given timelapse by quantifying the temporal evolution of the average signal intensity within control rectangular regions (of area $\simeq 3200\,\mu\mathrm{m}^2$) in the PSM, where the average intensity is not supposed to change in time. If significant bleaching was observed for a given sequence, a single exponential photobleaching curve was determined by nonlinear regression and a time dependent bleach correction factor was applied to measurements from that sequence. After photobleaching correction (if required), signal intensities at the somite boundary were normalized by the average intensity in the somite boundary before somite formation starts, namely within the [-60,-30] min time interval ($t = 0$ min corresponding to B-1).

### 4.6.6 Kymograph visualization of F-actin and myosin II signals at the somite boundary.

For each column corresponding to a time point in the sequence, the fluorescent actin (or myosin) signal was measured along the somite boundary by averaging intensities within a 3 $\mu$m diameter circular mask at an increment of 3 $\mu$m along the path specified by the annotated boundary. The kymograph shows the traced intensities along the boundary contour for each time frame (frame rate = 3 min).

### 4.6.7 Generation and injection of ferrofluid droplets.

Ferrofluid droplets were prepared as previously described [81, 77]. Briefly, DFF1 ferrofluid (Ferrotec) was diluted in filtered 3M Novec 7300 fluorocarbon oil. To prevent non-specific adhesion between cells and droplets, a fluorinated Krytox-PEG(600) surfactant (008-fluorosurfactant, RAN Biotechnologies [127]) was diluted in the ferrofluid at a 2.5% (w/w) concentration. A custom-made fluorous Cy5 dye was used to visualize the droplet (see below). The ferrofluid was calibrated before each experiment as previously described [81], so that the applied magnetic stresses are known. Once prepared and calibrated, the ferrofluid was injected into the lateral mesodermal progenitor zone between 4 and 6 somites stage to form droplets of approximately 30 µm in diameter, as previously described [81, 77]. Imaging of droplets started at least 1.5 hours after the injection to let the tissue fully recover from it. Embryos were incubated for 2 hours at 25°C following injection to allow for tissue recovery, as previously described [77].

### 4.6.8 Magnetic actuation of ferrofluid microdroplets.

Actuation of ferrofluid droplets was performed as previously described [81]. Briefly, ferrofluid droplets were actuated by a uniform and constant magnetic field to deform the droplet and apply stresses in the surrounding tissue. The magnetic field was applied for 20 minutes and subsequently turned off. The droplet interfacial tension $\gamma$ was measured in each experiment *in situ* and *in vivo* from these actuation experiments, as previously described [81, 77].

### 4.6.9 Generation of fluorinated cyanine dye for droplet imaging.

To visualize ferrofluid droplets and perform 3D stress measurements *in vivo* and *in situ*, we employed a custom-synthesized fluorous Cy5 dye. While fluorous Rhodamine dyes have been previously used to visualize droplets [81, 77], longer wavelength dyes are preferred for full 3D reconstructions of droplets. The fluorous Cy5 was synthesized using a similar protocol as previously described [128]. Briefly, a branched fluorous ketone was reacted with phenyl hydrazine to produce a fluorous indole. A fluorous methylene indolene was generated by $N$-alkylation with a perfluoroalkyl iodide. The heterocycle was condensed onto malonaldehyde bis(phenylimine) monohydrochloride in the presence of a pyridine base in acetic anhydride to generate the fluorous Cy5. The dye was isolated by column chromatography in 9% yield. The synthesized fluorous Cy5 dye was then diluted in the ferrofluid at a final concentration of 25 $\mu$M. We have previously show that the dye is biocompatible and enables robust 3D measurements of mechanical stresses [128].

### 4.6.10 Measurements of cell-scale and tissue-scale stresses.

Stresses were quantified from the deformations of droplets inserted in the tissues, as previously described [119, 77]. Briefly, droplets were imaged in 3D using confocal microscopy and their shape was reconstructed in 3D using automated software [119, 85]. Using the measured value of the interfacial tension for each droplet (see above) and the time evolution of the droplet geometry, we measured the time evolution of cell- and tissue-scale stresses, as detailed in reference [119]. Reported amplitudes of cell-scale stresses were obtained using the value $\alpha = 0.05$ in the analysis software [119] to remove the smallest and largest 5% values of stresses, as these extreme values are prone to noise.

### 4.6.11 Measurement of stresses at somite-somite boundaries.

The magnitude of stress anisotropy generated at the somite boundary was quantified by comparing the stresses along the somite boundary to the stresses in the direction perpendicular to the somite boundary. To do so, we measured the stresses in different surface regions on the droplet. At each time point, we defined a belt region as the set of droplet surface coordinates located within 5 µm of the somite boundary plane, which was identified by hand at each timepoint. We also defined anterior and posterior caps as the two 10 µm diameter regions on the droplet most distant from the somite-somite plane.

Let $H_{\mathrm{B}}$, $H_{\mathrm{A}}$, and $H_{\mathrm{P}}$ refer to the sets of mean curvature measurements within the belted region, the anterior cap, and the posterior cap, respectively. The boundary stress, $\sigma_{\mathrm{B}}$, reads

$$\sigma_{\mathrm{B}} = 2\gamma \left( H_{\mathrm{B}}^{\max} - \frac{\bar{H}_{\mathrm{A}} + \bar{H}_{\mathrm{P}}}{2} \right) , \tag{4.1}$$

where $\gamma$ is the droplet interfacial tension, $H_{\mathrm{B}}^{\mathrm{max}}$ is the maximal mean curvature value within the boundary belt, and $\bar{H}_{\mathrm{A}}$ and $\bar{H}_{\mathrm{P}}$ are the average mean curvatures in the anterior and posterior caps, respectively.

### 4.6.12 Quantification of T1 transition (neighbor exchange) rates.

To measure the spatiotemporal distribution in T1 transitions during somite formation, embryos featuring a membrane label were imaged at 1 minute intervals for at least 2 hours, as described above. Temporal alignment relative to B-1 was determined as described above. Each sequence was first divided into 10 minute increments, and then a quadrilateral grid was defined on the somite at that interval, as shown in Fig. 4.3a,b. The grid divides a forming somite into 9 segments along the ML direction and 5 segments along the AP direction. Moreover, the grid is extended further two rows anteriorly and posteriorly. All observed T1 transitions were recorded within the grid for each sequence, from S-2 to S2 and classified in 10 minute increments. The grid was used to define three regions within a forming somite: anterior boundary, somite interior, and posterior boundary. The anterior boundary region is the anterior-most row located within the somite, the posterior boundary region is the posterior-most row located inside the somite, and the somite interior region corresponds to the inner three rows between the anterior and posterior regions. T1 rates were computed within each region for each sequence. In total 14 somite formation sequences from 7 unique embryos were used. Measurements from all sequences were used to compute averages and standard errors.

### 4.6.13 Measurement of angles at the lateral boundary.

Measurements of angles between cells at the lateral boundary, both at the contact with the somite boundary and slightly anterior to it, were performed using FIJI [129], by obtaining the angle between two straight segments defined along the boundary.

### 4.6.14 Active foam simulation of somite formation.

To model somite formation, we adapted the theoretical framework of active foam simulations [120]. For initial configurations, a rectangular slab of cells that consists of eight prospective somites is generated with open boundary conditions. Each somite contains approximately 40 cells, 8 rows of cells in the ML direction and 5 rows of cells in the AP direction. Initial somite boundary is specified by assigning a somite ID to individual cells. To match experimentally observed initial somite boundary straightness, cell ID at the somite boundary is randomly swapped until the boundary straightness matches with the experimental value at stage B-3. As this region, the PSM, is close to confluence, we simulated the system at confluence throughout somite formation.

The equations governing the dynamics of the system are the same as in reference [120] and were integrated using the Euler-Maruyama method. The ramp up of heterotypic tension is implemented as a temporal increase of the target (fixed point) tension for heterotypic cell-cell contacts. The heterotypic tension ramp up was applied sequentially to somite boundaries and delayed by 30 minutes between them to match the experimentally observed time of somite formation. Throughout the simulations, T1 transitions were applied if a junctional length became shorter than a critical length, as previously described [120].

### 4.6.15 Statistics.

Unless otherwise stated, we calculated statistics by first averaging within a specified time window for each somite, and then computing ensemble statistics on values measured from different somites to obtain average and SE values at each time point. The sample size (number of somite boundaries) for analysis of boundary morphology and accumulation of actin and myosin was chosen so that the addition of new data points would not significantly change the findings and no data was excluded. For experiments involving stress and orientation measurements (Fig. 4.2d-h), droplets with diameters outside the range 24 to 36 µm were excluded from analysis. For direct measurements of boundary stress (Fig. 4.2j-l), all droplets located at the middle of the formed boundary were included.

### 4.6.16 Data availability.

Source data supporting these findings are available upon request.

### 4.6.17 Code availability.

The code developed for this manuscript is available upon request.

## 4.7 Permissions and Attributions

1. The content of chapter 4 is the result of a collaboration with Sangwoo Kim, Ben J. Gross, Ray Wu, Marie Pochitaloff, Irene Lim, Ellen M. Sletten and Otger Campàs. [1]. It is reproduced here in accordance with rights retained by the authors. To find the preprint version of this paper: `https://doi.org/10.1101/2021.03.27.437325`.

---

[1] E.R. Shelton, S. Kim, B.J. Gross, R. Wu, M. Pochitaloff, I. Lim, E.M. Sletten and O. Campàs bioRxiv 2021.03.27.437325

# Chapter 5

# Final Remarks and Future Directions

## 5.1 Final Remarks

The morphogenetic processes by which animals grow and take form have been a source of fascination for philosophers and scientists alike, from the time of Aristotle to the present day. Generations of technological advancement, dedicated experimentation, and developments in theory have elucidated the various mechanisms underlying developmental phenomena. We understand that cells contain genetic "blueprints" in the form of DNA, including ancient genetic programs which activate during development to specify the body plan and guide morphogenetic events. As development unfolds, cells respond to biochemical as well as mechanical cues from their local environment. These chemical and mechanical cues can induce and direct cell fate, direct cell movements, and generally modulate cellular activities. Spatial and temporal modulations in cellular activities ultimately give rise to the form of the embryo through the pattern of stresses generated, and the resulting strains realized according the mechanical properties of the tissue. To quote D'Arcy Thompson, "The form, then, of any portion of matter, whether it be living or dead, and the changes of form which are apparent in its movements and in its growth, may in all cases alike be described as due to the actions of force. In short, the form of an object is a 'diagram' of forces." [7] A century on from *On Growth and Form*, we are now taking part in an effort to determine these diagrams of forces within living matter, through visualization of cell activity and force associated proteins, model and simulation of mechanical processes, and a direct in vivo measurements of the forces themselves.

The notion that an object's form is mapped in some way to a diagram of forces lies at the heart of how droplet inclusions within tissues can reveal patterns of morphogenetic stress. As a virtually incompressible material, a droplet's volume will not contract or expand under changes in isotropic stress (i.e. pressure). However, anisotropies in stresses normal to the surface produce variations in local surface curvature, which may be observed and quantified. These variations in curvature can be related to stress anisotropies by the droplet surface interfacial tension. The development of a computational framework for automating the reconstruction of a droplet surface, analyzing its geometry, and computing meaningful stress metrics described in chapter 2 has been critical in advancing this technique. The code presented in chapter 2, and subsequent iterations, have enabled droplet based *in situ* stress measurements for multiple published[130, 77, 128] and on-going research efforts, *in vitro*, *ex vivo*, and *in vivo*. This research has expanded and will continue to expand our understanding of the roles of forces in shaping living tissues.

As we explored the role of forces in vertebrate axis elongation in chapter 3, we were confronted with the challenge faced by all materials undergoing transformation: how is the material made soft and pliable when sculpting is required, and how is it made sturdy and rigid to maintain the form achieved? In glass work, the artist heats the material in a glory hole to tune the mechanical properties to a point of workability. Upon cooling, the form is set. In zebrafish, yield stress measurements showed a spatial gradient in the material's "workability," raising the question as to how this was achieved. Our spatial and temporal analysis stresses within the MPZ and PSM help solve this puzzle. Within the framework of a jamming transition, we understand short-lived stress fluctuations at cell-cell junctions to be a fluidizing factor[120]. These active stresses work almost like an effective temperature to maintain the MPZ in a fluid-like state. As the cells from the MPZ are incorporated in the PSM, the decrease in extra-cellular space effectively jams the tissue, allowing the PSM to serve as a rigid substrate from which posterior growth may continue. In this way, the embryo is able to achieve uniaxial growth, effectively 3D printing itself, through maintenance of a spatial gradient in material properties.

The notion of a solid-like PSM anchoring growth is useful for understanding body axis elongation, but presents a challenge when we consider how somites are ultimately formed from this apparently hardened material. In chapter 4, we see how accumulation of F-actin and myosin II leads to increased stresses at the forming boundary, causing rapid straightening and localized fluidization. The ability to visualize and to quantify the morphogenetic stresses which give rise to somites using droplet force sensors in first-of-their-kind time-lapse studies was critical for establishing our physical understanding of the somite mechanical formations. Consistent with our findings in chapter 3, the magnitude of the stress anisotropy at the forming boundary exceeds the PSM yield stress value, allowing for local fluidization and plastic remodeling. Among the surprising findings was the experimental observation of a delay in myosin accumulation at the forming boundary relative to the straightening of the boundary. An explanation for the delay was found in the active foam simulations, performed by Sangwoo Kim, which suggest that various parameters of the cell tension set-points and fluctuation dynamics are configured so as to maximize boundary straightness while minimizing heterogeneities is somite forms. This mechanical picture of somite formation shows us how spatial and temporal tuning of the physical stresses generated by cells achieve robust formation of functional structures.

## 5.2 Future Directions

Understanding the role of mechanics in developmental biology continues to be an highly active field of research and droplet force sensor technology is currently being employed in many *in vivo*, *ex vivo*, and *in vitro* studies. As demonstrated in chapters 2 and 3, droplets allow us to quantify internal mechanical stresses generated during various key events in development. Such approaches can naturally be extended to studying events in regeneration and cancer.

In this thesis I have only characterized mechanical stresses associated with developmental processes in wild-type embryos. I suspect much could be learned by investigating how mechanical stresses are generated within homozygous knock-out animals displaying mutant developmental phenotypes. Genetic knockouts have been a powerful tool for learning about which genes are implicated in various developmental events. By studying the spatiotemporal characteristics of cell and tissue-scale stresses which lead to mutant phenotypes, we could obtain a better understand how genetics map to phenotypes, as well as how stresses shape both wild-type and mutant phenotypes.

Magnetically responsive oil droplets can also be used to apply mechanical stresses within tissues. In principal, this could be used to generate a mechanical perturbation. In certain developmental events, can a mechanical strain created by droplet actuation be used to enhance or repress expression of certain genes? If so, is there a dependence on the magnitude of stress or strain? Is this modulation of expression dependent on a particular functionalization of the droplet surface? Such an approach could be used to better understand how cells integrate the mechanical and chemical cues guiding decisions of cell-fate and morphogenetic movements.

# Bibliography

[1] S. F. Gilbert, *Developmental Biology, 10th Edition.* Sinauer Associates, Inc., 2014.

[2] A. M. Turing, *The chemical basis of morphogenesis*, *Philosophical Transactions of the Royal Society B: Biological Sciences* **237** (1952), no. 641 37–72.

[3] M. A. Basson, *Signaling in cell differentiation and morphogenesis*, *Cold Spring Harbor Perspectives in Biology* **4** (2012), no. 6 1–21.

[4] T. Mammoto and D. E. Ingber, *Mechanical control of tissue and organ development*, 2010.

[5] O. Campàs, T. Mammoto, S. Hasso, R. A. Sperling, D. O'Connell, A. G. Bischof, R. Maas, D. A. Weitz, L. Mahadevan, and D. E. Ingber, *Quantifying cell-generated mechanical forces within living embryonic tissues*, *Nature methods* **11** (2014), no. 2 183–189.

[6] B. Bénazéraf and O. Pourquié, *Formation and Segmentation of the Vertebrate Body Axis*, *Annual review of cell and developmental biology* **29** (Oct., 2013) 1–26.

[7] D. W. Thompson, *On Growth and Form.* Cambridge: at the University Press, 1917.

[8] Aristotle. and A. L. Peck, *Generation of animals, with an English translation by A.L. Peck.* Harvard University Press, 1943.

[9] S. Reynolds, *Cooking up the perfect insect: Aristotle's transformational idea about the complete metamorphosis of insects*, *Philosophical Transactions of the Royal Society B: Biological Sciences* **374** (2019), no. 1783.

[10] J. Maienschein, *Epigenesis and Preformationism*, in *The Stanford Encyclopedia of Philosophy* (E. N. Zalta, ed.). Metaphysics Research Lab, Stanford University, spring 2017 ed., 2017.

[11] W. Roux, *Beiträge zur Entwickelungsmechanik des Embryo*, *Archiv für mikroskopische Anatomie* **29** (1887), no. 1 157–212.

[12] H. Driesch, *The potency of the first two cleavage cells in echinoderm development. experimental production of partial and double formation (reprinted translation)*, *Zeitschrift für wissenschafliche Zoologie* **53** (1892) 160–178.

[13] J.-B. Lamarck, *Zoological Philosophie.* 1914.

[14] C. Darwin, *On the Origin of the Species.* 1859.

[15] E. Haeckel, *Generelle Morphologie der Organsimen.* Berlin: George Reimer, 1867.

[16] T. H. Morgan, *Chromosomes and Heredity*, *The American Naturalist* **XLIV** (1910), no. 524 449–496.

[17] F. Griffith, *The significance of pneumococcal types*, *Journal of Hygiene* **27** (1928), no. 2 113–159.

[18] O. T. Avery, C. M. Macleod, and M. McCarty, *Studies on the chemical nature of the substance inducing transformation of pneumococcal types: Induction of transformation by a desoxyribonucleic acid fraction isolated from pneumococcus type iii*, *Journal of Experimental Medicine* **79** (1944), no. 2 137–158.

[19] A. D. Hershey and M. Chase, *Independent functions of viral protein and nucleic acid in growth of bacteriophage*, *Journal of General Physiology* **36** (sep, 1952) 39–56.

[20] J. D. Watson and F. H. C. Crick, *Molecular structure of nucleic acids*, *Nature* **171** (1953), no. 4356 737–738.

[21] R. E. Franklin and R. Gosling, *Molecular configuration of Sodium Thymonucleate*, *Nature* **171** (1953), no. 4356 740–741.

[22] F. Crick, L. Barnett, S. Brenner, and R. Watts-Tobin, *General nature of the genetic code for proteins*, *Nature* **192** (1961), no. 4809 1227–1232.

[23] J. Monod, J.-P. Changeux, and F. Jacob, *Allosteric proteins and cellular control systems*, *Journal of Molecular Biology* **6** (1963), no. 4 306–329.

[24] S. Gould, *Ontogeny and Phylogeny.* Harvard University Press, Cambridge, 1977.

[25] F. Jacob, *Evolution and tinkering*, *Science* **196** (1977), no. 4295 1161–1166.

[26] A. M. Maxam and W. Gilbert, *A new method for sequencing DNA. 1977.*, *Proceedings of the National Academy of Sciences* **74** (1977), no. 2 560–564.

[27] S. F. Gilbert, *The morphogenesis of evolutionary developmental biology*, *International Journal of Developmental Biology* **47** (2003), no. 7-8 467–477.

[28] E. Lewis, *A gene complex controlling segmentation in drosophila*, *Nature* **276** (1978), no. 5688 565–570.

[29] L. A. Davidson, G. F. Oster, R. E. Keller, and M. A. Koehl, *Measurements of mechanical properties of the blastula wall reveal which hypothesized mechanisms of primary invagination are physically plausible in the sea urchin Strongylocentrotus purpuratus*, *Developmental Biology* **209** (may, 1999) 221–238.

[30] C. Bertet, L. Sulak, and T. Lecuit, *Myosin-dependent junction remodelling controls planar cell intercalation and axis elongation*, *Nature* **429** (jun, 2004) 667–671.

[31] M. Behrndt, G. Salbreux, P. Campinho, R. Hauschild, F. Oswald, J. Roensch, S. W. Grill, and C.-P. Heisenberg, *Forces Driving Epithelial Spreading in Zebrafish Gastrulation*, *Science* **338** (oct, 2012) 257–260.

[32] C. M. Nelson, R. P. Jean, J. L. Tan, W. F. Liu, N. J. Sniadecki, A. A. Spector, and C. S. Chen, *Emergent patterns of growth controlled by multicellular form and mechanics*, *Proceedings of the National Academy of Sciences of the United States of America* **102** (2005), no. 33 11594–11599.

[33] C. M. Nelson, M. M. VanDuijn, J. L. Inman, D. A. Fletcher, and M. J. Bissell, *Tissue geometry determines sites of mammary branching morphogenesis in organotypic cultures*, *Science* **314** (2006), no. 5797 298–300.

[34] E. J. Arnsdorf, P. Tummala, R. Y. Kwon, and C. R. Jacobs, *Mechanically induced osteogenic differentiation - The role of RhoA, ROCKII and cytoskeletal dynamics*, *Journal of Cell Science* **122** (2009), no. 4 546–553.

[35] A. Mammoto, K. M. Connor, T. Mammoto, C. W. Yung, D. Huh, C. M. Aderman, G. Mostoslavsky, L. E. H. Smith, and D. E. Ingber, *A mechanosensitive transcriptional mechanism that controls angiogenesis*, *Nature* **457** (2009), no. 7233 1103–1108.

[36] R. Farhadifar, J. C. Röper, B. Aigouy, S. Eaton, and F. Jülicher, *The Influence of Cell Mechanics, Cell-Cell Interactions, and Proliferation on Epithelial Packing*, *Current Biology* **17** (dec, 2007) 2095–2104.

[37] G. Scarcelli, W. J. Polacheck, H. T. Nia, K. Patel, A. J. Grodzinsky, R. D. Kamm, and S. H. Yun, *Noncontact three-dimensional mapping of intracellular hydromechanical properties by Brillouin microscopy*, *Nature Methods* **12** (2015), no. 12 1132–1134.

[38] M. Krieg, Y. Arboleda-Estudillo, P.-H. Puech, J. Käfer, F. Graner, D. J. Müller, and C.-P. Heisenberg, *Tensile forces govern germ-layer organization in zebrafish*, *Nature Cell Biology* **10** (apr, 2008) 429–436.

[39] O. Campàs, *A toolbox to explore the mechanics of living embryonic tissues*, *Seminars in Cell  Developmental Biology* **55** (2016) 119–130. Telocytes Tissue morphodynamics.

[40] P. Roca-Cusachs, V. Conte, and X. Trepat, *Quantifying forces in cell biology*, *Nature Cell Biology* **19** (2017), no. 7 742–751.

[41] S. W. Grill, P. Gönczy, E. H. K. Stelzer, and A. A. Hyman, *Polarity controls forces governing asymmetric spindle positioning in the Caenorhabditis elegans embryo*, *Nature* **409** (2001), no. 6820 630–633.

[42] R. Schlüßler, S. Möllmert, S. Abuhattum, G. Cojoc, P. Müller, K. Kim, C. Möckel, C. Zimmermann, J. Czarske, and J. Guck, *Mechanical Mapping of Spinal Cord Growth and Repair in Living Zebrafish Larvae by Brillouin Imaging*, *Biophysical Journal* **115** (sep, 2018) 911–923.

[43] D. R. Soll, *Computer-assisted three-dimensional reconstruction and motion analysis of living, crawling cells*, *Computerized medical imaging and graphics* (1999).

[44] D. R. Soll, E. Voss, O. Johnson, and D. Wessels, *Three-dimensional reconstruction and motion analysis of living, crawling cells*, *Scanning* (2000).

[45] T. S. Ursell, J. Nguyen, R. D. Monds, A. Colavin, G. Billings, N. Ouzounov, Z. Gitai, J. W. Shaevitz, and K. C. Huang, *Rod-like bacterial shape is maintained by feedback between cell curvature and cytoskeletal localization*, *Proceedings of the National Academy of Sciences* **111** (Mar., 2014) E1025–E1034.

[46] T. Hayashi and R. W. Carthew, *Surface mechanics mediate pattern formation in the developing retina*, *Nature* (Sept., 2004) 1–6.

[47] T. Lecuit and P. F. Lenne, *Cell surface mechanics and the control of cell shape, tissue patterns and morphogenesis*, *Nature Reviews Molecular Cell Biology* (2007).

[48] A. Pierre, J. Sallé, M. Wühr, and N. Minc, *Generic Theoretical Models to Predict Division Patterns of Cleaving Embryos*, *Developmental Cell* (2016).

[49] R. Wang, A. Kamgoue, C. Normand, and I. Léger-Silvestre, *High resolution microscopy reveals the nuclear shape of budding yeast during cell cycle and in various biological states*, *J Cell Sci* (2016).

[50] D.-H. Kim, B. Li, F. Si, J. M. Phillip, D. Wirtz, and S. X. Sun, *Volume regulation and shape bifurcation in the cell nucleus.*, *Journal of Cell Science* **128** (Sept., 2015) 3375–3385.

[51] J. Zhou, S. Long, Q. Wang, and A. D. Dinsmore, *Measurement of forces inside a three-dimensional pile of frictionless droplets.*, *Science* **312** (June, 2006) 1631–1633.

[52] J. Brujić, S. F. Edwards, D. V. Grinev, I. Hopkinson, D. Brujić, and H. A. Makse, *3D bulk measurements of the force distribution in a compressed emulsion system*, *Faraday Discussions* **123** (Oct., 2002) 207–220.

[53] G. W. Brodland, J. H. Veldhuis, S. Kim, M. Perrone, D. Mashburn, and M. S. Hutson, *CellFIT: A Cellular Force-Inference Toolkit Using Curvilinear Cell Boundaries*, *PLOS ONE* **9** (June, 2014) e99116.

[54] J. H. Veldhuis, A. Ehsandar, J.-L. Maître, T. Hiiragi, S. Cox, and G. W. Brodland, *Inferring cellular forces from image stacks*, *Philosophical Transactions of the Royal Society B: Biological Sciences* **372** (Mar., 2017) 20160261.

[55] M. Delarue, F. Ingremeau, J. Prost, A. Delon, M. E. Dolega, and G. Cappello, *Cell-like pressure sensors reveal increase of mechanical stress towards the core of multicellular spheroids under compression*, *Nature communications* **8** (Jan., 2017) 1–9.

[56] N. Otsu, *A Threshold Selection Method from Gray-Level Histograms*, *IEEE Transactions on Systems, Man, and Cybernetics* **9** (1979), no. 1 62–66.

[57] S. Beucher and C. Lantuéjoul, "Use of watersheds in contour detection." International Workshop on Image Processing: Real-time Edge and Motion Detection/Estimation, Sept., 1979.

[58] W. E. Lorensen and H. E. Cline, *Marching cubes: A high resolution 3D surface construction algorithm*, *ACM siggraph computer graphics* (1987).

[59] M. Kass, A. Witkin, and D. Terzopoulos, *Snakes: Active contour models*, *International journal of computer vision* (1988).

[60] P. T. Sander and S. W. Zucker, *Inferring surface trace and differential structure from 3-D images*, *IEEE Transactions on Pattern Analysis . . .* (1990).

[61] A. R. Evans, I. S. Harper, and G. D. Sanson, *Confocal imaging, visualization and 3-D surface measurement of small mammalian teeth.*, *Journal of microscopy* **204** (Nov., 2001) 108–118.

[62] O. Dzyubachyk, W. A. van Cappellen, J. Essers, W. J. Niessen, and E. Meijering, *Advanced Level-Set-Based Cell Tracking in Time-Lapse Fluorescence Microscopy*, *IEEE Transactions on Medical Imaging* **29** (2010), no. 3 852–867.

[63] E. S. Welf, M. K. Driscoll, K. M. Dean, C. Schäfer, and J. Chu, *Quantitative multiscale cell imaging in controlled 3D microenvironments*, *Developmental Cell* (2016).

[64] H. Elliott, R. S. Fischer, K. A. Myers, R. A. Desai, and L. Gao, *Myosin II controls cellular branching morphogenesis and migration in three dimensions by minimizing cell-surface curvature*, *Nature cell ...* (2015).

[65] A. Bovik, ed., *Handbook of Image and Video Processing.* Academic Press, July, 2005.

[66] M. J. Rust, M. Bates, and X. Zhuang, *Sub-diffraction-limit imaging by stochastic optical reconstruction microscopy (STORM)*, *Nature methods* (2006).

[67] V. S. Nalwa and T. O. Binford, *On detecting edges*, *IEEE Transactions on Pattern Analysis ...* (1986).

[68] J. Ye, G. Fu, and U. P. Poudel, *High-accuracy edge detection with blurred edge model*, *Image and vision computing* (2005).

[69] F. Aguet, M. Jacob, and M. Unser, *Three-dimensional feature detection using optimal steerable filters*, in *IEEE International Conference on Image Processing*, 2005.

[70] T. D. Gatzke and C. M. Grimm, *Estimating curvature on triangular meshes*, *International journal of shape modeling* (2006).

[71] E. Kalogerakis, D. Nowrouzezahrai, P. Simari, and K. Singh, *Extracting lines of curvature from noisy point clouds*, *Computer-Aided Design* **41** (Apr., 2009) 282–292.

[72] Q. Mérigot, M. Ovsjanikov, and L. J. Guibas, *Voronoi-Based Curvature and Feature Estimation from Point Clouds*, *IEEE Transactions on Visualization and Computer Graphics* **17** (2011), no. 6 743–756.

[73] S. Fleishman, D. Cohen-Or, and C. T. Silva, *Robust Moving Least-squares Fitting with Sharp Features*, in *ACM Transactions on Graphics*, pp. 544–552, July, 2005.

[74] A. Gray, *Modern differential geometry of curves and surfaces with Mathematica.* CRC Press, Boca Raton, FL, 2nd ed., Jan., 1997.

[75] A. A. Lucio, D. E. Ingber, and O. Campas, *Generation of biocompatible droplets for in vivo and in vitro measurement of cell-generated mechanical stresses*, *Methods in cell biology* (2015).

[76] C. Schröter, L. Herrgen, A. Cardona, G. J. Brouhard, B. Feldman, and A. C. Oates, *Dynamics of zebrafish somitogenesis*, *Developmental Dynamics* **237** (2008), no. 3 545–553.

[77] A. Mongera, P. Rowghanian, H. J. Gustafson, E. Shelton, D. A. Kealhofer, E. K. Carn, F. Serwane, A. A. Lucio, J. Giammona, and O. Campàs, *A fluid-to-solid jamming transition underlies vertebrate body axis elongation*, *Nature* **561** (2018), no. 7723 401–405.

[78] C. Nüsslein-Volhard and R. Dahm, *Zebrafish: A Practical Approach.* Oxford University Press, 2002.

[79] K. R. Mosaliganti, R. R. Noche, F. Xiong, I. A. Swinburne, and S. G. Megason, *ACME: Automated Cell Morphology Extractor for Comprehensive Reconstruction of Cell Membranes*, *PLoS Computational Biology* **8** (2012), no. 12.

[80] Z. Lele, A. Folchert, M. Concha, G. J. Rauch, R. Geisler, F. Rosa, S. W. Wilson, M. Hammerschmidt, and L. Bally-Cuif, *Parachute/ n-cadherin is required for morphogenesis and maintained integrity of the zebrafish neural tube*, *Development* **129** (2002), no. 14 3281–3294.

[81] F. Serwane, A. Mongera, P. Rowghanian, D. A. Kealhofer, A. A. Lucio, Z. M. Hockenbery, and O. Campàs, *In vivo quantification of spatially varying mechanical properties in developing tissues*, *Nature Methods* **14** (2017), no. 2 181–186.

[82] C. Holtze, A. C. Rowat, J. J. Agresti, J. B. Hutchison, F. E. Angilè, C. H. Schmitz, S. Köster, H. Duan, K. J. Humphry, R. A. Scanga, J. S. Johnson, D. Pisignano, and D. A. Weitz, *Biocompatible surfactants for water-in-fluorocarbon emulsions*, *Lab on a Chip* (2008).

[83] E. M. Sletten and T. M. Swager, *Fluorofluorophores: Fluorescent fluorous chemical tools spanning the visible spectrum*, *Journal of the American Chemical Society* (2014).

[84] J. Rallison, *The Deformation of Small Viscous Drops and Bubbles in Shear Flows*, *Annual Review of Fluid Mechanics* (1984).

[85] E. Shelton, F. Serwane, and O. Campàs, *Geometrical characterization of fluorescently labelled surfaces from noisy 3D microscopy data*, *Journal of Microscopy* **269** (2018), no. 3 259–268.

[86] T. Tabata and Y. Takei, *Morphogens, their identification and regulation*, *Development (Cambridge, England)* **131** (Feb., 2004) 703–712.

[87] G. A. Stooke-Vaughan and O. Campas, *Physical control of tissue morphogenesis across scales*, *Current opinion in genetics & development* **51** (Oct., 2018) 111–119.

[88] C.-P. Heisenberg and Y. Bellaiche, *Forces in Tissue Morphogenesis and Patterning*, *Cell* **153** (May, 2013) 948–962.

[89] C. Guillot and T. Lecuit, *Mechanics of Epithelial Tissue Homeostasis and Morphogenesis*, *Science (New York, NY)* **340** (June, 2013) 1185–1189.

[90] A. Hubaud and O. Pourquié, *Signalling dynamics in vertebrate segmentation*, *Nature reviews Molecular cell biology* (Oct., 2014) 1–13.

[91] M.-L. Dequéant and O. Pourquié, *Segmental patterning of the vertebrate embryonic axis.*, *Nature reviews Genetics* **9** (May, 2008) 370–382.

[92] O. Pourquié, *Vertebrate Somitogenesis*, in *Annual Review of Cell and Developmental Biology*, vol. 17, pp. 311–350, 2001.

[93] O. Pourquié, *The segmentation clock: Converting embryonic time into spatial pattern*, *Science* **301** (2003), no. 5631 328–330.

[94] Y. J. Jiang, B. L. Aerne, L. Smithers, C. Haddon, D. Ish-Horowicz, and J. Lewis, *Notch signalling and the synchronization of the somite segmentation clock*, *Nature* **408** (2000), no. 6811 475–479.

[95] O. F. Venzin and A. C. Oates, *What are you synching about? Emerging complexity of Notch signaling in the segmentation clock*, 2020.

[96] A. C. Oates, L. G. Morelli, and S. Ares, *Patterning embryos with oscillations: structure, function and dynamics of the vertebrate segmentation clock.*, *Development (Cambridge, England)* **139** (Feb., 2012) 625–639.

[97] A. Mara and S. A. Holley, *Oscillators and the emergence of tissue organization during zebrafish somitogenesis.*, *Trends in cell biology* **17** (Dec., 2007) 593–599.

[98] J. Cooke and E. C. Zeeman, *A clock and wavefront model for control of the number of repeated structures during animal morphogenesis*, *Journal of Theoretical Biology* **58** (1976), no. 2 455–476.

[99] L. Durbin, C. Brennan, K. Shiomi, J. Cooke, A. Barrios, S. Shanmugalingam, B. Guthrie, R. Lindberg, and N. Holder, *Eph signaling is required for segmentation and differentiation of the somites.*, *Genes & development* **12** (Oct., 1998) 3096–3109.

[100] Y. Nakaya, S. Kuroda, Y. T. Katagiri, K. Kaibuchi, and Y. Takahashi, *Mesenchymal-epithelial transition during somitic segmentation is regulated by differential roles of Cdc42 and Rac1*, *Developmental Cell* **7** (2004), no. 3 425–438.

[101] T. Watanabe, Y. Sato, D. Saito, R. Tadokoro, and Y. Takahashi, *EphrinB2 coordinates the formation of a morphological boundary and cell epithelialization during somite segmentation*, *Proceedings of the National Academy of Sciences of the United States of America* **106** (2009), no. 18 7467–7472.

[102] C. Dahmann, A. C. Oates, and M. Brand, *Boundary formation and maintenance in tissue development*, *Nature Reviews Genetics* **12** (jan, 2011) 43–55.

[103] D. Jülich, A. P. Mould, E. Koper, and S. A. Holley, *Control of extracellular matrix assembly along tissue boundaries via integrin and Eph/Ephrin signaling*, *Development* **136** (2009), no. 17 2913–2921.

[104] S. Lackner, J. Schwendinger-Schreck, D. Jülich, and S. A. Holley, *Segmental Assembly of Fibronectin Matrix Requires rap1b and integrin $\alpha 5$*, *Developmental Dynamics* **242** (2013), no. 2 122–131.

[105] P. McMillen, V. Chatti, D. Jülich, and S. A. Holley, *A sawtooth pattern of cadherin 2 stability mechanically regulates somite morphogenesis*, *Current Biology* **26** (2016), no. 4 542–549.

[106] S. R. Naganathan and A. C. Oates, *Patterning and mechanics of somite boundaries in zebrafish embryos*, *Seminars in Cell and Developmental Biology* (2020), no. March 1–9.

[107] S. Tlili, J. Yin, J. F. Rupprecht, M. A. Mendieta-Serrano, G. Weissbart, N. Verma, X. Teng, Y. Toyama, J. Prost, and T. E. Saunders, *Shaping the zebrafish myotome by intertissue friction and active stress*, *Proceedings of the National Academy of Sciences of the United States of America* **116** (2019), no. 51 25430–25439.

[108] J. B. Bard, *A traction-based mechanism for somitogenesis in the chick*, *Roux's Archives of Developmental Biology* **197** (1988), no. 8 513–517.

[109] D. S. Packard and A. G. Jacobson, *Analysis of the physical forces that influence the shape of chick somites*, *Journal of Experimental Zoology* **207** (1979), no. 1 81–92.

[110] A. S. Dias, I. De Almeida, J. M. Belmonte, J. A. Glazier, and C. D. Stern, *Somites without a clock*, *Science* **343** (2014), no. 6172 791–795.

[111] S. R. Naganathan, M. Popovic, and A. C. Oates, *Somite deformations buffer imprecise segment lengths to ensure left-right symmetry*, *bioRxiv* (2020) 2020.08.14.251645.

[112] F. Gallaire and P.-T. Brun, *Fluid dynamic instabilities: theory and application to pattern forming in complex media.*, *Philosophical transactions. Series A, Mathematical, physical, and engineering sciences* **375** (May, 2017).

[113] D. Umetsu, B. Aigouy, M. Aliee, L. Sui, S. Eaton, F. Jülicher, and C. Dahmann, *Local Increases in Mechanical Tension Shape Compartment Boundaries by Biasing Cell Intercalations*, *Current Biology* **24** (Aug., 2014) 1798–1805.

[114] K. P. Landsberg, R. Farhadifar, J. Ranft, D. Umetsu, T. J. Widmann, T. Bittig, A. Said, F. Jülicher, and C. Dahmann, *Increased Cell Bond Tension Governs Cell Sorting at the Drosophila Anteroposterior Compartment Boundary*, *Current Biology* **19** (2009), no. 22 1950–1955.

[115] B. Monier, A. Pélissier-Monier, A. H. Brand, and B. Sanson, *An actomyosin-based barrier inhibits cell mixing at compartmental boundaries in Drosophila embryos*, *Nature Cell Biology* **12** (2010), no. 1 60–65.

[116] R. J. Major and K. D. Irvine, *Localization and requirement for myosin II at the dorsal-ventral compartment boundary of the Drosophila wing*, *Developmental Dynamics* **235** (2006), no. 11 3051–3058.

[117] S. Koshida, Y. Kishimoto, H. Ustumi, T. Shimizu, M. Furutani-Seiki, H. Kondoh, and S. Takada, *Integrin$\alpha$5-dependent fibronectin accumulation for maintenance of somite boundaries in zebrafish embryos*, *Developmental Cell* **8** (2005), no. 4 587–598.

[118] A. Barrios, R. J. Poole, L. Durbin, C. Brennan, N. Holder, and S. W. Wilson, *Eph/Ephrin signaling regulates the mesenchymal-to-epithelial transition of the paraxial mesoderm during somite morphogenesis.*, *Current Biology* **13** (Sept., 2003) 1571–1582.

[119] B. Gross, E. Shelton, C. Gomez, and O. Campàs, *Stress, an automated geometrical characterization of deformable particles for in vivo measurements of cell and tissue mechanical stresses*, *bioRxiv* (2021).

[120] S. Kim, M. Pochitaloff, G. Stooke-Vaughan, and O. Campàs, *Embryonic Tissues as Active Foams*, *Nature Physics* **X** (2021), no. X X.

[121] J. V. Veenvliet, A. Bolondi, H. Kretzmer, L. Haut, M. Scholze-Wittler, D. Schifferl, F. Koch, L. Guignard, A. S. Kumar, M. Pustet, S. Heimann, R. Buschow, L. Wittler, B. Timmermann, A. Meissner, and B. G. Herrmann, *Mouse embryonic stem cells self-organize into trunk-like structures with neural tube and somites.*, *Science (New York, NY)* **370** (Dec., 2020).

[122] D. Jülich, G. Cobb, A. M. Melo, P. McMillen, A. K. Lawton, S. G. J. Mochrie, E. Rhoades, and S. A. Holley, *Cross-Scale Integrin Regulation Organizes ECM and Tissue Topology*, *Developmental cell* **34** (July, 2015) 33–44.

[123] I. A. Swinburne, K. R. Mosaliganti, S. Upadhyayula, T. L. Liu, D. G. Hildebrand, T. Y. Tsai, A. Chen, E. Al-Obeidi, A. K. Fass, S. Malhotra, F. Engert, J. W. Lichtman, T. Kirchhausen, E. Betzig, and S. G. Megason, *Lamellar projections in the endolymphatic sac act as a relief valve to regulate inner ear pressure*, *eLife* **7** (2018) 1–34.

[124] J. Compagnon, V. Barone, S. Rajshekar, R. Kottmeier, K. Pranjic-Ferscha, M. Behrndt, and C. P. Heisenberg, *The notochord breaks bilateral symmetry by controlling cell shapes in the Zebrafish laterality organ*, *Developmental Cell* **31** (2014), no. 6 774–783.

[125] J. L. Maître, H. Berthoumieux, S. F. G. Krens, and G. Salbreux, *Adhesion functions in cell sorting by mechanically coupling the cortices of adhering cells*, *Science* (2012).

[126] O. Pourquié and P. P. Tam, *A nomenclature for prospective somites and phases of cyclic gene expression in the presomitic mesoderm*, *Developmental cell* **1** (2001), no. 5 619–620.

[127] C. Holtze, A. C. Rowat, J. J. Agresti, J. B. Hutchison, F. E. Angile, C. H. J. Schmitz, S. Koster, H. Duan, K. J. Humphry, R. A. Scanga, J. S. Johnson, D. Pisignano, and D. A. Weitz, *Biocompatible surfactants for water-in-fluorocarbon emulsions*, *Lab On A Chip* **8** (2008), no. 10 1632–1639.

[128] I. Lim, A. Vian, H. L. van de Wouw, R. A. Day, C. Gomez, Y. Liu, A. L. Rheingold, O. Campas, and E. M. Sletten, *Fluorous Soluble Cyanine Dyes for Visualizing Perfluorocarbons in Living Systems*, *Journal of the American Chemical Society* **142** (Aug., 2020) 16072–16081.

[129] J. Schindelin, I. Arganda-Carreras, E. Frise, V. Kaynig, M. Longair, T. Pietzsch, S. Preibisch, C. Rueden, S. Saalfeld, B. Schmid, J.-Y. Tinevez, D. J. White, V. Hartenstein, K. Eliceiri, P. Tomancak, and A. Cardona, *Fiji: an open-source platform for biological-image analysis.*, *Nature Methods* **9** (June, 2012) 676–682.

[130] A. A. Lucio, A. Mongera, E. Shelton, R. Chen, A. M. Doyle, and O. Campàs, *Spatiotemporal variation of endogenous cell-generated stresses within 3D multicellular spheroids.*, *Nature Publishing Group* **7** (2017), no. 1 12022.